University of Alberta

"A nonideal Statistical Rate Theory of Evaporation using equations of state"
AND "Lattice Boltzmann simulations and analytical solutions of pulsating flows in ducts"

by

ATAM KAPOOR ©

A thesis submitted to the Faculty of Graduate Studies and Research
in partial fulfillment of the requirements for the degree of

Master of Science

in

Chemical Engineering

Department of Chemical & Materials Engineering

Edmonton, Alberta
Fall 2008

Library and Archives Canada

Published Heritage Branch

395 Wellington Street
Ottawa ON K1A 0N4
Canada

Bibliothèque et Archives Canada

Direction du Patrimoine de l'édition

395, rue Wellington
Ottawa ON K1A 0N4
Canada

Your file Votre référence
ISBN: 978-0-494-47276-7
Our file Notre référence
ISBN: 978-0-494-47276-7

NOTICE:
The author has granted a non-exclusive license allowing Library and Archives Canada to reproduce, publish, archive, preserve, conserve, communicate to the public by telecommunication or on the Internet, loan, distribute and sell theses worldwide, for commercial or non-commercial purposes, in microform, paper, electronic and/or any other formats.

The author retains copyright ownership and moral rights in this thesis. Neither the thesis nor substantial extracts from it may be printed or otherwise reproduced without the author's permission.

AVIS:
L'auteur a accordé une licence non exclusive permettant à la Bibliothèque et Archives Canada de reproduire, publier, archiver, sauvegarder, conserver, transmettre au public par télécommunication ou par l'Internet, prêter, distribuer et vendre des thèses partout dans le monde, à des fins commerciales ou autres, sur support microforme, papier, électronique et/ou autres formats.

L'auteur conserve la propriété du droit d'auteur et des droits moraux qui protège cette thèse. Ni la thèse ni des extraits substantiels de celle-ci ne doivent être imprimés ou autrement reproduits sans son autorisation.

In compliance with the Canadian Privacy Act some supporting forms may have been removed from this thesis.

While these forms may be included in the document page count, their removal does not represent any loss of content from the thesis.

Conformément à la loi canadienne sur la protection de la vie privée, quelques formulaires secondaires ont été enlevés de cette thèse.

Bien que ces formulaires aient inclus dans la pagination, il n'y aura aucun contenu manquant.

Canada

Abstract

The use of statistical mechanics to explain thermodynamics and fluid mechanics as a result of the underlying microscopic interactions is one of the active research areas in chemical engineering. In this thesis, the application of two such statistical mechanical models, namely Statistical Rate Theory and Lattice Boltzmann model is presented. Previously existing ideal Statistical Rate Theory is extended to incorporate nonideal fluid behavior to develop a generic equation-of-state based model for predicting evaporation rates. This model is free from any fitting parameters and hence can be incorporated into a thermodynamic simulator. Also, in this thesis, a fluid mechanical problem of oscillating incompressible flows in rectangular ducts is studied using Lattice Boltzmann simulations and analytically in annular ducts. Stress analysis of duct walls is done to identify high-stress regions, an understanding of which is very useful in the study of critical medical conditions like hypertension and dialysis.

Acknowledgements

This thesis work has been an epoch changing event of my life. It is the result of two years of research whereby I matured socially, technically and academically. It is always said that the journey of a thousand miles begins with a single step. Today, I feel delighted to get this opportunity to write a testament to the steps I covered during the last two years whereby I was assisted, guided and supported by many people. It is a delectable moment for me to express my gratitude for all the people who provided me with their expertise, making this sojourn, an enriching and a great learning experience.

I am highly indebted to my supervisors, Dr. Phillip Choi (Professor, University of Alberta) and Dr. Janet Elliott (Professor, University of Alberta) with whom I have been working since September 2006, when I joined the MSc. program at the Department of Chemical and Materials Engineering at the University of Alberta. Their expertise in the field of thermodynamics and statistical mechanics has been a great value for me. Their patience, understanding and strong enthusiasm for research has been a great motivation for me. Their encouragement, guidance and stimulating suggestions in spite of their busy schedule, has helped me to think logically and focus on solutions to the problems rather than problems themselves. I fall short of words to thank them enough for their interest and efforts.

I would also like to give my special thanks to Dr. Franz h.c. Durst (Head of Institute, Institute of Fluid Mechanics, University of Erlangen-Nurnberg, Germany) and Dr. Kamen Beronov (Research Scientist, Institute of Fluid Mechanics, University of Erlangen-Nurnberg, Germany) for introducing me to the topic of statistical mechanical simulations, especially Lattice Boltzmann simulations. It is their expertise, guidance and the perspective of research which made a deep impression on me and encouraged me to recognize my field of research interest.

I would also like to thank my friends and lab group members who supported me socially and academically making the environment conducive for research.

I would like to express my gratitude for my family members for their patient love, support and understanding which helped me to be reckoned at a stage I am at, today.

Finally, I would like to thank the Department of Chemical and Materials Engineering at the University of Alberta and the Natural Sciences and Engineering Research Council of Canada (NSERC) for providing me the financial support during my entire graduate program.

Table of Contents

1 Introduction 1

1.1 Motivation 1

1.2 Thesis outline 5

1.3 References 7

2 A nonideal Statistical Rate Theory formulation to predict evaporation rates from equations of state 10

2.1 Introduction 10

2.2 Statistical Rate Theory for evaporation - A review 12

2.2.1 Evaporation rate expression 12

2.2.2 Entropy change calculation 17

2.2.3 Equilibrium molecular exchange rate 19

2.3 Ideal SRT 21

2.3.1 Ideal gas approximation 21

2.3.2 Incompressible liquid treatment 23

2.3.3 Ideal SRT expression 24

TABLE OF CONTENTS

2.4 Statistical Rate Theory - Nonideal corrections 26

2.4.1 Departure functions for chemical potential and enthalpy 26

2.4.2 Nonideal corrections to the equilibrium molecular exchange rate . 27

2.4.3 An example - The Peng-Robinson equation of state 31

2.5 Results 35

2.5.1 Comparison with previous experiments 35

2.5.2 Further predictions based on Peng-Robinson SRT 35

2.6 Conclusions 40

2.7 References 41

3 Lattice Boltzmann simulations for asymptotic incompressible flow profiles with a periodic pressure gradient 44

3.1 Introduction 44

3.2 The Lattice Boltzmann equation - A review 47

3.2.1 The Boltzmann equation 47

3.2.2 The Lattice Boltzmann equation 49

3.3 Computational issues 54

3.3.1 Boundary conditions 55

3.3.2 Force evaluation 57

3.4 Pulsating flow in a duct - The problem 57

3.5 Results 59

3.5.1 Low frequency flow 60

3.5.2 High frequency flow 63

TABLE OF CONTENTS

3.5.3 Stress at high frequencies 66

3.6 Conclusions 69

3.7 References 70

4 Exact solution for circumferentially pulsating annular flow with a constant radial flux **74**

4.1 Introduction 74

4.2 Method 76

4.2.1 Steady flow 78

4.2.2 Oscillating flow 80

4.3 Results and discussion 84

4.3.1 Low frequency flows 85

4.3.2 High frequency flows 88

4.4 Conclusions 90

4.5 References 91

5 Conclusions and Future Work **93**

5.1 Conclusion 93

5.2 Future work 95

5.3 References 98

List of Figures

2.1 Schematic of a steady-state evaporation system (adapted from Figure 1 in Ref. [16]). Assume that the macroscopic curvature only affects the pressure difference across the interface; however, in a sub-volume, Gibbs Dividing Surface approximation has been applied. 13

2.2 Schematic diagram of a hypothetical surface. 28

2.3 Using the experimentally measured values of the radius of curvature and the temperatures on both sides of the interface for water (from Tables I and II in Ref. [16]), vapor pressures have been predicted using the ideal [16] and the Peng-Robinson based SRT model that would result in the experimentally measured evaporation flux. The predicted values of the vapor pressure for both models have been plotted on the ordinate, against the experimentally measured vapor pressure values on the abscissa. The points will lie on the 45^o line, if they are in perfect agreement. 34

2.4 Using the experimentally measured values of the radius of curvature and the temperatures on both sides of the interface for octane (from Table I in Ref. [17]), vapor pressures have been predicted using the ideal [17] and the Peng-Robinson based SRT model that would result in the experimentally measured evaporation flux. The predicted values of the vapor pressure for both models have been plotted on the ordinate, against the experimentally measured vapor pressure values on the abscissa. The points will lie on the 45^o line, if they are in perfect agreement. 36

2.5 Predictions for ethane at $T = 25^oC$ and $T = 30^oC$ made using both the ideal and the Peng-Robinson based SRT model after assuming a zero temperature jump at the interface, have been shown. The predicted values of the vapor pressure for both the models have been plotted on the ordinate, against the evaporation flux on the abscissa. Deviations can be seen for high flux values. 37

2.6 Predictions for butane at $T = 400K$ made using both the ideal and the Peng-Robinson based SRT models after assuming a zero temperature jump at the interface, have been shown. The predicted values of the vapor pressure for both the models have been plotted on the ordinate, against the evaporation flux on the abscissa. Deviations can be seen for high flux values. 38

2.7 The Peng-Robinson based SRT model was used to predict the vapor pressure for a liquid temperature of $400K$ for butane assuming temperature jumps of 0 and $2K$ across the interface. The predicted values of the vapor pressure for zero temperature difference across the interface are plotted on the ordinate, against the predicted vapor pressure values for a temperature jump of $2K$ across the interface, on the abscissa. If they were in perfect agreement, they lie on the 45^o line. 39

LIST OF FIGURES

3.1 Schematic of a typical 2-dimensional 9-discrete lattice velocity (D2Q9) lattice in a 2D Lattice Boltzmann calculation. Each lattice node contains 9 cells, each of which stores a particle distribution function corresponding to the particular lattice velocity assigned to the cell. 50

3.2 Lattice velocities of the D2Q9 (left) and D3Q19 (right) models. 51

3.3 A schematic showing the collision time step (left) followed by a streaming time step (right) in a D2Q9 lattice model. Black (left) and red (right) color nodes represent that the pre-collision and post-collision values of the distribution function respectively. 54

3.4 A schematic showing the importance of boundary conditions for the D2Q9 model. For near-wall nodes, the collision step is incomplete as there are no fluid nodes in the wall and so post-collision distribution function values can not be updated for the near-wall nodes. 56

3.5 Schematic of a rectangular duct across which a pulsating pressure drop is applied. 58

3.6 3-D cross-sectional (resolution 20 x 20) velocity profiles at four different times for low frequency velocity solution with 1536 time steps. The velocity profile is of parabolic type and the centre-most point achieves the maximum amplitude during a period. 60

3.7 3-D cross-sectional (resolution 20 x 20) velocity profiles at four different times for low frequency velocity solution with 576 time steps. The development of annular effects [12] can be seen in the second quadrant and the velocity profile starts exhibiting a Stokesian nature. 62

3.8 Phase difference between velocity and pressure gradient for *Top Left:* Low frequency (1536 timesteps, phase difference: 0.17π), *Top Right:* Moderate frequency (768 timesteps, phase difference: 0.28π), *Bottom Left:* High frequency (576 timesteps, phase difference: 0.35π) and *Bottom Right:* Very High frequency (96 timesteps, phase difference: 0.5π). 63

3.9 3-D cross-sectional velocity profiles at four different times for high frequency velocity solution with 96 time steps. Annular effects and flattening effects are significant and the centre-most point no longer achieves the maximum velocity amolitude. 64

3.10 3-D cross-sectional (resolution: 40 x 40) velocity profiles at four different times for high frequency velocity solution with 48 time steps. Annular effects and flattening effects are significant and sharp velocity gradients develop near the wall. 65

3.11 Normalized stress from the analytical solution (light points) by Drake [12] and from the LB simulation (dark triangles) have been plotted on the abscissa against the normalized distance on the ordinate. As is evident from the plot, that the LB simulation results are in close agreement with the analytical solution. 67

3.12 Phase difference between stress and pressure gradient for *Top Left:* Low frequency (1536 timesteps, phase difference: 0.13π), *Top Right:* Moderate frequency (768 timesteps, phase difference: 0.19π), *Bottom Left:* High frequency (576 timesteps, phase difference: 0.22π) and *Bottom Right:* Very High frequency (96 timesteps, phase difference: 0.25π). 68

4.1 Schematic representation of a cylindrical annulus with porous walls (radial flux with injection at the inner wall (R_1) and suction at the outer wall (R_2)) and a circumferentially oscillating pressure gradient across the longitudinal direction. 77

4.2 Low Womersley number, low Reynolds number: Non-dimensional velocity amplitude $\tilde{u}_\theta$ (Top) and phase angle distributions ϕ (Bottom) for three different aspect ratios ($\lambda = 1.2, 1.5, 2$) have been plotted for the low frequency oscillating flow solution (Womersley number, $\alpha = 0.1$) for a solid walled annulus (Radial Reynolds number, $\beta = 0$). 84

4.3 Low Womersley number, high Reynolds number: Non-dimensional velocity amplitude $\tilde{u}_\theta$ (Top) and phase angle distributions ϕ (Bottom) for three different aspect ratios ($\lambda = 1.2, 1.5, 2$) have been plotted for the low frequency oscillating flow solution (Womersley number, $\alpha = 0.1$) for a radially permeable annulus (Radial Reynolds number, $\beta = 30$). 86

4.4 High Womersley number, low Reynolds number: Non-dimensional velocity amplitude $\tilde{u}_\theta$ (Top) and phase angle distributions ϕ (Bottom) for three different aspect ratios ($\lambda = 1.2, 1.5, 2$) have been plotted for the high frequency oscillating flow solution (Womersley number, $\alpha = 15$) for a solid walled annulus (Radial Reynolds number, $\beta = 0$). 87

4.5 High Womersley number, high Reynolds number: Non-dimensional velocity amplitude $\tilde{u}_\theta$ (Top) and phase angle distributions ϕ (Bottom) for an aspect ratio of $\lambda = 2$ have been plotted for a high frequency oscillating flow solution with a Womersley number α of 15. The radial Reynolds number based on the radial velocity β ranges from 0 to 100 to study the convection effects in the flow region. 88

Chapter 1

Introduction

1.1 Motivation

Modeling of fluids is an active area of research in chemical engineering, driven by it's necessity in understanding industrial phenomena. Conventional continuum fluid models were developed to describe the macroscopic properties of a fluid, building on the concepts of classical physics. Numerical methods have been used in the past to solve complex differential equations for simple systems which model the fluid without using the information that it is made of atoms. But, as the need to improve on the understanding of fluid phenomena and solutions for unsolved and partly solved complex flow problems were realized, attempts were made to explain the behavior of macroscopic systems from a microscopic or a molecular point of view. This led to the use of statistical mechanics in developing models to explain and predict macroscopic phenomena of moving fluids from the properties of the individual atoms making up the system; thereby, explaining fluid mechanics and thermodynamics as a natural result of statistics, quantum and classical

mechanics.

The techniques of statistical mechanics have been applied extensively to chemical, physical and biological systems including: gases, liquids, electrolytic solutions, colloids, interfaces, complex fluids, polymers and biopolymers, helix-coil transition of DNA, cell membrane transport phenomena etc. There are four main techniques to use statistical information to compute transport properties of fluids: Molecular dynamics (MD), Monte-Carlo (MC) techniques, Statistical Rate Theory (SRT) and Lattice Boltzmann (LB) models.

Molecular dynamics (MD) follows the time evolution of particles by integrating their equations of motion. Molecular dynamics simulations calculate the net force on the particles by considering the interaction forces among the particles and the external forces to determine the acceleration of the particle as a function of time. Integrating the equations of motion generates information at the microscopic level including spatial positions and velocities of the particles making up the system as functions of time. Using this information, the state of the system can be predicted at any time in the future, and macroscopic properties like pressure, energy, volume, heat capacity etc. can be calculated. However, molecular dynamics simulations are time consuming and computationally expensive as they track the spatial and velocity coordinates of all the molecules making up the system at time intervals of the order of a femtosecond. Molecular dynamics has been applied in the past to processes ranging from adsorption of hydrogen in carbonaceous micro-porous materials [1] to determination of structures from x-ray crystallography [2] to biochemical processes like conformational changes in proteins [3, 4] and nucleic acids [5].

Statistical Rate Theory (SRT) was first proposed in 1977 [6] with its more complete form in 1982 [7, 8, 9, 10] and since then, has been used to predict rates of various kinetic processes like gas absorption at liquid-gas interfaces, electron transfer reactions between ionic isotopes, gas adsorption on solid substrates, thermal desorption of CO from Ni(111)

and liquid evaporation. Unlike other classical kinetic theory models like Absolute Rate Theory, which are based on the concept of precursor states or sticking probability, SRT is based on a first order perturbation analysis of the Schrödinger equation between quantum mechanical energy states. Statistical Rate Theory solves for the rate of kinetic processes by assuming them to be mainly consisting of single-molecular events. Thus, the Schrödinger equation for the system is solved before and after the transition of a molecule from one phase to the other, and using the two solutions of the Schrödinger equation, the net transition probability of the molecule is determined. Upon integrating over time and particle numbers, one can determine the net rate of the thermodynamic process being studied. Since the final rate expression obtained in the SRT formulation is free from any fitting parameters, SRT is a very powerful technique and computationally inexpensive.

However, in all the applications of the Statistical Rate Theory, the gaseous phase has been assumed to be ideal and the liquid and the solid phases to be incompressible. No attempts until now, have been made to incorporate nonidealities into the SRT formulation. The objective of this study is to develop a method to include nonideal effects in the Statistical Rate Theory (SRT) formulation to develop a generic equation-of-state based SRT model for predicting the kinetic rate processes. Evaporation is taken as an example to study the nonideal SRT model that has been developed.

The Lattice Boltzmann (LB) equation based model is a relatively new fluid-dynamics simulation technique for complex fluid systems. Unlike the traditional CFD methods, which solve the conservation equations of macroscopic properties (i.e., mass, momentum, and energy) numerically, LB models are based on statistical mechanics and allow the particles to move on a discrete lattice. Local collisions conserve mass and momentum; however, it was found that the hydrodynamic solutions are very noisy and on a macroscopic scale, some additional force terms are seen in the Navier-Stokes equation which is derived by integrating the microscopic scale collision equations to a macroscopic scale. It was later realized that instead of fluid particles, a local density distribution should be allowed to advect, thereby eliminating the noise and the additional terms in Navier-Stokes equations.

There on, this model has been successfully applied to applications including turbulence [11, 12] , multi-component flows [13], and multi-phase systems [14, 15], to name a few.

Due to their particulate nature and local dynamics, LB models have several advantages over conventional computational fluid dynamics (CFD) methods, especially in dealing with complex boundaries, incorporating of microscopic interactions, and parallelization of the algorithm. LB models are at least as robust, accurate and computationally efficient as traditional methods of computation. In the last decade, LB models have been extensively used to investigate problems like crystallization, magnetohydrodynamics, etc. However, there is a need to study oscillating flows which are very fundamental to biochemical flow phenomena using LB methods. In biochemical flow problems like arterial-capillary flows and blood flow in kidney-dialysis bags, oscillating flows are present in micro-sized tubules; therefore macroscopic hydrodynamic flow equations yield inaccurate results giving rise to a need to examine them using microscopic models like LB and MD. There is a conspicuous lack of information on how stress behaves as the oscillating frequency changes. Stress analysis of oscillating flows is very useful for designing medical apparatuses like peristaltic pumps, kidney-dialysis bags, and to study medical conditions like hypertension. The objective of this work is to study velocity and stress behavior as functions of the oscillating frequency of the pressure gradient in a 3-D rectangular duct. Velocity and stress behavior in different parts of the channel will be followed until the asymptotic profiles are achieved to understand the development of various trends in the profiles as the oscillating frequency is increased.

The primary objective of this thesis is to understand the theory of two of these new computational methods (LB method and SRT) based on statistical mechanics to comprehend the effects of microscopic constituents and interactions on the macroscopic transport properties of a fluid. Evaporation rate prediction and pulsating incompressible flow in a rectangular duct were studied to understand the use of these statistical methods in a thermodynamic and a fluid-mechanical process respectively.

1.2 Thesis outline

Evaporation is a very fundamental process in the chemical industry and is widely seen in applications ranging from separation processes [16] to handling. Until now, evaporation has been studied mainly from a fluid-mechanical point of view where the rate of evaporation is dictated by correlation studies including mass-transfer coefficients. The purpose of this study is to develop an expression for the rate of evaporation from a thermodynamic point of view using equations of state. Chapter 2 of the thesis reviews the Statistical Rate Theory (SRT) formulation for evaporation and extends it by incorporating nonidealities into the previously existing ideal SRT expression. A generic equation-of-state based SRT model is developed which can be used in all ranges of temperature and pressure and is written only in terms of thermodynamic variables which can be measured experimentally or calculated from the equations of state.

Chapter 3 of the thesis presents the Lattice Boltzmann (LB) simulation theory for pulsating incompressible flow in a finite length channel. Pulsating flows play an important role in many engineering applications including medical science and biological engineering [17, 18]. Periodic flows appear in various medical apparatuses which are used for fluid delivery and testing like peristaltic pumps, heart-lung machines, suction therapy equipment, and extra-corporeal circulation. Pulsating flows have applications for blood flow in fiber membranes used for dialysis in the artificial kidney. Understanding stress variations in pulsating flows due to periodic pressure gradients is fundamentally significant for the design and optimization of such medical apparatuses. The oscillating flow of an incompressible viscous fluid in long channels has been investigated in detail for different geometries both experimentally and analytically. However, there is a conspicuous lack of information on the velocity and stress behavior of pulsating flows. In chapter 3, the velocity and stress behavior of pulsating flows have been investigated as a function of the oscillating frequency of the periodic pressure gradient using Lattice Boltzmann simulations.

1. Introduction

In the literature, analytical solutions for laminar, fully developed, oscillating flow in rectangular ducts have been studied previously in great detail. A large number of investigations have been focused on analyzing Newtonian viscous and incompressible flows in straight ducts with both permeable and impermeable walls. However, since most of the mechanical systems involving pulsating flows are cylindrical or annular in nature, for example in medical apparatuses, understanding cell transport process dynamics, and artificial dialysis bags; there is a need to develop exact solutions of the hydrodynamic equations in cylindrical coordinates. In chapter 4, we develop an exact solution of the Navier-Stokes equations for the incompressible flow in an annulus with porous walls, when an oscillating circumferential pressure gradient is applied.

Finally, a conclusion of all these theories and formulations is summarized in chapter 5 of the thesis. Some future work possibilities and ideas have also been presented.

References

[1] Georgakis,M.; Stavropoulosa, G.; Sakellaropoulosa, G.P. *International Journal of Hydrogen Energy*, **2007**, 32(12), 1999.

[2] Richardson, R.C.; King, N.M.; Harrington, D.J.; Sun, H.; Royer, W.E.; Nelson, D.J. *Protein Sci.*, **2000**, 9, 73.

[3] Gsponer, J.; Caflisch, A. *Proceedings of the National Academy of Sciences of the United States of America*, **2002**, 99(10), 6719.

[4] Fersht, A.R. *Proceedings of the National Academy of Sciences of the United States of America*, **2002**, 99(22), 14122.

[5] Cheatham III, T. E.; Kollman, P.A. *Annual Review of Physical Chemistry*, **2000**, 51, 435.

[6] Ward, C. A. *J. Chem. Phys.*, **1977**, 67, 229.

REFERENCES

[7] Ward, C. A.; Findlay, R. D.; Rizk, M. *J. Chem. Phys.*, **1982**, 76(11), 5599.

[8] Ward, C. A.; Rizk, M.; Tucker, A. S. *J. Chem. Phys.*, **1982**, 76, 5606.

[9] Ward, C. A.; Findlay, R. D. *J. Chem. Phys.*, **1982**, 76, 5615.

[10] Findlay, R. D.; Ward, C. A. *J. Chem. Phys.*, **1982**, 76, 5624.

[11] Benzi, R.; Succi, S. *J. Phys. A: Math. Gen.*, **1990**, 23, L1-L5.

[12] Filippova, O.; Succi, S.; Mazzocco, F.; Arrighetti, C.; Bella, G.; Hnel, D. *Journal of Computational Physics*, **2001**, 170(2), 812.

[13] Dupin M.M.; Halliday I.; Care C.M. *Journal of Physics A: Mathematical and General*, **2003**, 36(31), 8517.

[14] Teng, S.; Chen, Y.; Ohashi, H. *International Journal of Heat and Fluid Flow*, **2000**, 21(1), 112.

[15] Zheng, H. W.; Shu, C.; Chew, Y.T. *Journal of Computational Physics*, **2006**, 218(1), 353.

[16] Freitas, S.; Merkle, H.P.; Bruno Gander; B. *Journal of Controlled Release*, **2005**, 102(2), 313.

REFERENCES

[17] Hsiai T.K.; Cho S.K.; Honda H.M.; Hama S.; Navab M.; Demer L.L.; Ho C.M. *Annals of Biomedical Engineering*, **2002**, 30(5), 646.

[18] Kharnas, S. Sh.; Lokshin, M. A.; Mogilevskii, E. B.; Smirnov, L. S. *J. Biomedical Engineering*, **1982**, 16(1), 1573.

Chapter 2

A nonideal Statistical Rate Theory formulation to predict evaporation rates from equations of state [1]

2.1 Introduction

Recent experimental measurements have found that the temperature on the vapor side of an evaporating liquid is higher than the temperature on the liquid side. Temperature jumps of 5-8 K have been observed [1]. This can not be explained by models based on classical kinetic theory [2] which predict liquid evaporation only if the vapor temperature is less than the temperature on the liquid side. This is because all of these models

[1] This chapter is reproduced with permission from A. Kapoor and J. A. W. Elliott, "A nonideal Statistical Rate Theory formulation to predict evaporation rates from equations of state", Journal of Physical Chemistry, in press. Unpublished work copyright 2008 American Chemical Society.

assume the boundary condition of the temperature of the molecules evaporating to be the temperature of the liquid and thus the solutions generated are opposite to the experimental observations.

Since classical kinetic theory models were shown to fail, quantum mechanical models of isolated thermodynamic systems were developed to explain the observations. A new model called Statistical Rate Theory (SRT) [3, 4, 5], based on the concept of transition probability was used to investigate the observations. This model uses the Boltzmann definition of entropy and the equilibrium exchange rate to obtain the SRT expression for predicting kinetic rates of various processes in terms of measurable molecular and material variables. Statistical Rate Theory assumes the transport processes to be primarily single-molecular events and is then developed using a first-order perturbation analysis of the Schrödinger equation. To date, over 75 papers have been published on this theory. Statistical Rate Theory has been used in the past to predict rates for various processes ranging from gas absorption at liquid-gas interfaces [6], gas adsorption on solid substrates [4, 5, 7, 8, 9, 10], electron transfer between ions in solution [4, 11], migration of CO across a stepped Pt(111) surface [12], crystal growth from solution [13] and transport across cell membranes [14, 15]. Ward and Fang [16, 17] used the SRT model to predict the evaporation rates of water and hydrocarbons and explained the unexpected temperature jump across the interface.

However, in all these applications, the SRT model has always been implemented by assuming ideality of gaseous phases and the incompressibility of solid/ liquid phases. Even the experiments measuring the temperature jump [1] across the interface have been at sufficiently low temperatures and pressures that the ideal SRT model was in close agreement with the experimental results. This is because the nonideal and compressibility effects could be accurately neglected and so no attempt was made to incorporate fluid bulk-phase nonidealities in the SRT expressions.

In this chapter, a method to incorporate nonidealities using equations of state in the SRT model is presented and a general expression for any equation of state is given. Further, the Peng-Robinson equation of state (fairly accurate for hydrocarbons) has been taken as an example and predictions have been made using both the Peng-Robinson SRT model and the ideal SRT model to identify the region where the two models differ. The rest of the chapter is organized as follows: In Section 2.2, a review of the Statistical Rate Theory approach for predicting evaporation rates. In Section 2.3, the ideal assumptions made by Ward and Fang [16, 17] to predict evaporation rates are presented. In Section 2.4, an equation of state in the SRT model is introduced and a generic evaporation rate expression is developed. In Section 2.5, results are presented and further predictions are made to identify the range where nonideal effects are expected. Finally, in Section 2.6 concluding remarks are presented.

2.2 Statistical Rate Theory for evaporation - A review

In this section, a review of the development of Statistical Rate Theory [3, 4] and specifically SRT applied to evaporation [16, 17] is presented.

2.2.1 Evaporation rate expression

Consider an isolated C-component thermodynamic system containing a liquid bulk phase and a vapor bulk phase with a liquid-vapor interface in between. Using the Gibbs Dividing Surface approximation for the interface, it is assumed that a molecule can only be in the liquid or the vapor phase. Suppose that the system is not in equilibrium i.e. the number of molecules in the vapor and the liquid are different from their equilibrium values. Consider an isolated element of the system obtained by dividing the system into small but finite

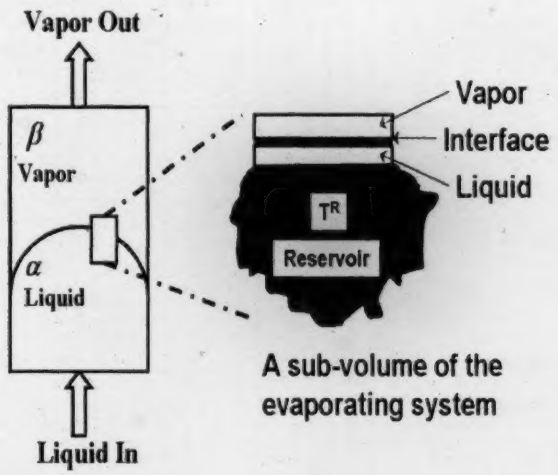

Figure 2.1: Schematic of a steady-state evaporation system (adapted from Figure 1 in Ref. [16]). Assume that the macroscopic curvature only affects the pressure difference across the interface; however, in a sub-volume, Gibbs Dividing Surface approximation has been applied.

sub-volumes as shown in Figure 2.1. Let α and β denote the liquid and the vapor phases in the sub-volume, respectively. Let, at any instant t, the molecular configuration of the system, λ_j be given as

$$\lambda_j\left(N_\alpha, N_\beta\right) \; : \; \left(N_\alpha^1, N_\alpha^2, N_\alpha^3, ..., N_\alpha^\gamma, ...N_\alpha^C\right), \left(N_\beta^1, N_\beta^2, N_\beta^3, ..., N_\beta^\gamma, ...N_\beta^C\right)$$

where N_α^i and N_β^i are the number of molecules of component i in the liquid and the vapor phase, respectively. Statistical Rate Theory predicts the rate at which component γ is transfered from the liquid phase to the vapor phase.

2. A nonideal Statistical Rate Theory formulation to predict evaporation rates from equations of state

Let $\hat{H}_0$ and $\hat{H}$ denote the Hamiltonian operator for the system when molecules are in the state λ_j, i.e. confined in their sub-volume phases (unperturbed state), and when the molecules are free to move across the interface between the sub-volume phases (perturbed state), respectively. A potential operator $\hat{V} \equiv \hat{H} - \hat{H}_0$ can be defined, which allows the molecules to interact with their actual potential. The Schrödinger equation for the system when the molecules are allowed to move freely across the interface becomes:

$$\frac{h}{i}\frac{\partial \psi}{\partial t} = \left(\hat{H}_0 + \hat{V}\right)\psi \tag{2.1}$$

where ψ is the wave function for the liquid-vapor system. To apply perturbation theory, it is assumed that $\frac{|\hat{V}\,\psi|}{|\hat{H}_0\,\psi|}$ is very small; however, this assumption is different from saying that $\hat{V}$ is zero, because in that case the molecules would stay in their confined state, thereby making the transition probability zero. Considering the energy uncertainty principle, eigenfunctions x_0^r corresponding to the unperturbed Hamiltonian within an energy uncertainty ΔE can be determined from

$$\hat{H}_0\, x_0^r = E_0^r\, x_0^r \tag{2.2}$$

where E_0 is the energy eigenvalue. These energy eigenvalues are highly degenerate. Corresponding to a molecular distribution λ_j, there are $\Omega(\lambda_j)$ quantum mechanical states. Thus, there are $\Omega(\lambda_j)$ wave functions which correspond to the same molecular distribution and so the wave function of the unperturbed liquid-vapor system can be written as a linear

combination of all the possible $\Omega(\lambda_j)$ wave functions as

$$\psi = \sum_{r}^{\Omega(\lambda_j)} C_r \, x_0^r \exp\left(\frac{-i}{\hbar} E_0^r t\right) \tag{2.3}$$

where the C_r are linear coefficients. The system may be in any of the $\Omega(\lambda_j)$ quantum mechanical states. In writing this, it is assumed that the system is equally likely to be in any of the quantum mechanical states within an energy uncertainty, ΔE, an assumption similar to Gibbs "principle of equal *a priori* probabilities" in statistical thermodynamics, however, here applied to a thermodynamic system not in equilibrium. At this instant, the system has a transition probability to move to a molecular configuration resulted by the transfer of one molecule (of component γ) from the liquid phase α to the vapor phase β. Assume at this point that the number of molecules in other sub-volumes does not change during this transition. This configuration λ_k will be given as:

$$\lambda_k \left(N_\alpha - 1, N_\beta + 1\right) \; : \; \left(N_\alpha^1, N_\alpha^2, N_\alpha^3, ..., N_\alpha^\gamma - 1, ...N_\alpha^C\right), \\ \left(N_\beta^1, N_\beta^2, N_\beta^3, ..., N_\beta^\gamma + 1, ...N_\beta^C\right)$$

If the number of quantum mechanical states corresponding to this molecular distribution is given by $\Omega(\lambda_k)$, then according to the standard perturbation analysis, the probability of a transition from molecular distribution λ_j to λ_k is given as

$$\tau\left(\lambda_j \rightarrow \lambda_k\right) = K\left(\lambda_j, \lambda_k\right) \frac{\Omega(\lambda_k)}{\Omega(\lambda_j)} \tag{2.4}$$

where

$$K(\lambda_j, \lambda_k) = \frac{2\pi}{\hbar}\omega_j |V_{mn}|^2 \tag{2.5}$$

where ω_j and V_{mn} are the microscopic state density of molecular configuration λ_j and matrix elements of the operator $\hat{V}$, respectively.

At the same instant, there is a possibility of a single molecular transition in the opposite sense, to the molecular configuration, λ_p.

$$\lambda_p(N_\alpha + 1, N_\beta - 1) : \left(N_\alpha^1, N_\alpha^2, N_\alpha^3, ..., N_\alpha^\gamma + 1, ...N_\alpha^C\right), \left(N_\beta^1, N_\beta^2, N_\beta^3, ..., N_\beta^\gamma - 1, ...N_\beta^C\right)$$

The transition probability from λ_j to the configuration λ_p is given as

$$\tau(\lambda_j \rightarrow \lambda_p) = K(\lambda_j, \lambda_p)\frac{\Omega(\lambda_p)}{\Omega(\lambda_j)} \tag{2.6}$$

where

$$K(\lambda_j, \lambda_p) = \frac{2\pi}{\hbar}\omega_j |V_{ms}|^2 \tag{2.7}$$

where ω_j and V_{ms} are the microscopic state density of molecular configuration λ_j and matrix elements of the operator $\hat{V}$, respectively.

Combining Equations 2.4 and 2.6, the net rate of the forward process (evaporation) can be written as

$$J_{\alpha\beta} = K(\lambda_j, \lambda_k)\frac{\Omega(\lambda_k)}{\Omega(\lambda_j)} - K(\lambda_j, \lambda_p)\frac{\Omega(\lambda_p)}{\Omega(\lambda_j)} \tag{2.8}$$

Introducing the Boltzmann definition of entropy, $S(\lambda_d) = k \ln \Omega(\lambda_d)$, where k is the Boltzmann constant, the numbers of microstates in Equation 2.8 can be replaced by the entropy of the states, yielding the final expression for the rate of molecular transfer from phase α to β [3, 4]:

$$J_{\alpha\beta} = K(\lambda_j, \lambda_k)\exp\left[\frac{S(\lambda_k) - S(\lambda_j)}{k}\right] - K(\lambda_j, \lambda_p)\exp\left[\frac{S(\lambda_p) - S(\lambda_j)}{k}\right] \tag{2.9}$$

2.2.2 Entropy change calculation

Since entropy is an extensive quantity, the additive property of entropy can be used to write the total entropy change during the transition as the sum of entropy changes for the liquid (α), vapor (β) and the reservoir (R):

$$S(\lambda_k) - S(\lambda_j) = \sum_{i=\alpha,\beta,R} [S^i(\lambda_k) - S^i(\lambda_j)] \tag{2.10}$$

2. A nonideal Statistical Rate Theory formulation to predict evaporation rates from equations of state

Using Euler relations [18], the entropy change in Equation 2.10 may be written as [16]:

$$S(\lambda_k) - S(\lambda_j) = \left(\frac{H^\alpha(\lambda_k)}{T^\alpha} - \frac{H^\alpha(\lambda_j)}{T^\alpha}\right) + \left(\frac{H^\beta(\lambda_k)}{T^\beta} - \frac{H^\beta(\lambda_j)}{T^\beta}\right) + \left(\frac{\mu^\alpha}{T^\alpha} - \frac{\mu^\beta}{T^\beta}\right) + \left(\frac{H^R(\lambda_k)}{T^\alpha} - \frac{H^R(\lambda_j)}{T^\alpha}\right) \tag{2.11}$$

where H, T and μ are the enthalpy, temperature and the chemical potential of the phase, respectively. It has been assumed that intensive thermodynamic variables remain unchanged as a result of a single molecular event. Since an isolated system is considered, there is no net energy change during the molecular transition event. Thus, the energy balance equation for the isolated system can be written as:

$$[H^\alpha(\lambda_k) - H^\alpha(\lambda_j)] + \left[H^\beta(\lambda_k) - H^\beta(\lambda_j)\right] + [H^R(\lambda_k) - H^R(\lambda_j)] = 0 \tag{2.12}$$

Substituting Equation 2.12 in Equation 2.11 yields

$$S(\lambda_k) - S(\lambda_j) = \left(\frac{\mu^\alpha}{T^\alpha} - \frac{\mu^\beta}{T^\beta}\right) + \left(\frac{1}{T^\beta} - \frac{1}{T^\alpha}\right)\left[H^\beta(\lambda_k) - H^\beta(\lambda_j)\right] \tag{2.13}$$

The enthalpy per molecule h is now introduced by using $H^i = h^i N^i$ to replace $\left[H^\beta(\lambda_k) - H^\beta(\lambda_j)\right]$ in Equation 2.13 by $h^\beta \Delta N^\beta = h^\beta$ (the transition causes a change of one molecule, so $\Delta N^\beta = 1$) to obtain the final expression for entropy change as [16]

$$S(\lambda_k) - S(\lambda_j) = \left(\frac{\mu^\alpha}{T^\alpha} - \frac{\mu^\beta}{T^\beta}\right) + h^\beta\left(\frac{1}{T^\beta} - \frac{1}{T^\alpha}\right) \tag{2.14}$$

Since the entropy change in the reverse process (from configuration λ_j to λ_p) is simply the negative of the entropy change in Equation 2.14,

$$S(\lambda_p) - S(\lambda_j) = -[S(\lambda_k) - S(\lambda_j)] \tag{2.15}$$

2.2.3 Equilibrium molecular exchange rate

To develop thermodynamic expressions for the K's, consider the system in the limit of equilibrium when the entropy difference between the states before and after the transition approaches zero. Thus, the rate in Equation 2.9 becomes

$$J_{\alpha\beta} = K(\lambda_e, \lambda_f) - K(\lambda_e, \lambda_b) \tag{2.16}$$

where λ_e is the equilibrium molecular configuration, and λ_f and λ_b are molecular configurations on either side of the equilibrium configuration. At equilibrium, although the system is subject to these fluctuations in the molecular configuration, the net rate $J_{\alpha\beta}$ should be zero. Thus, from Equation 2.16,

$$K(\lambda_e, \lambda_f) = K(\lambda_e, \lambda_b) = K_e \tag{2.17}$$

This means that $K(\lambda_e, \lambda_f)$ is independent of the direction of the transition and does not depend on the molecular configurations. Since, for molecular distributions near equi-

librium, $K(\lambda_j, \lambda_k)$ is independent of the distributions λ_j and λ_k, this property of K to all near-equilibrium molecular transitions [3, 4] can be generalized, i.e.

$$\begin{aligned} K(\lambda_{e+s}, \lambda_{e+s-1}) = K(\lambda_{e+s-1}, \lambda_{e+s-2}) = ... = K(\lambda_{e+1}, \lambda_e) = K(\lambda_e, \lambda_{e-1}) \\ = K(\lambda_{e-1}, \lambda_{e-2}) = ... = K(\lambda_{e-h}, \lambda_{e-h-1}) = K_e \end{aligned} \tag{2.18}$$

where K_e is the equilibrium value. Since the K's are independent of the initial and final states, they represent the reversible part in the rate expression in Equation 2.9 and the entropy terms in the rate expression can be considered to give rise to irreversibility.

Since at equilibrium, the uni-directional rate of molecular transport from phase α to phase β is $\overrightarrow{J_{\alpha\beta}} = K_e$ and from phase β to phase α is $\overrightarrow{J_{\beta\alpha}} = K_e$, it follows that K_e is the uni-directional equilibrium molecular exchange rate between the two phases. Thus, K_e is a function of the equilibrium properties of the system.

Thus, substituting Equations 2.14, 2.15 and 2.18 into Equation 2.9 gives the final expression for the rate for evaporation as [16]:

$$\begin{aligned} J_{\alpha\beta} = K_e \Bigg\{ & \exp\left[\frac{\mu^\alpha}{kT^\alpha} - \frac{\mu^\beta}{kT^\beta} + \frac{h^\beta}{k}\left(\frac{1}{T^\beta} - \frac{1}{T^\alpha}\right)\right] \\ & - \exp\left[-\frac{\mu^\alpha}{kT^\alpha} + \frac{\mu^\beta}{kT^\beta} - \frac{h^\beta}{k}\left(\frac{1}{T^\beta} - \frac{1}{T^\alpha}\right)\right] \Bigg\} \end{aligned} \tag{2.19}$$

2.3 Ideal SRT

In section 2.3, a review of the ideal treatment of the fluid phases in the previous application of Statistical Rate Theory to evaporation [16] is presented.

2.3.1 Ideal gas approximation

To evaluate the expression for the net rate of evaporation obtained in the previous section (Equation 2.19), expressions for the equilibrium molecular exchange rate (K_e), chemical potentials and specific enthalpies are needed. Considering Boltzmann statistics and the Born-Oppenheimer approximation, translational, vibrational, rotational and electronic partition functions of an ideal gas can be written as [19, 20]

$$q_{trans} = \left(\frac{2\pi mkT}{h^2}\right)^{3/2} V = \frac{V}{\Lambda^3} \tag{2.20}$$

$$q_{vib} = \prod_{l=1}^{N_v} \frac{\exp(-\theta_l/2T)}{1-\exp(-\theta_l/T)} \tag{2.21}$$

$$q_{rot} = \left(\frac{2kT}{h^2}\right)^{3/2} \frac{(\pi I)^{1/2}}{\sigma_s} \tag{2.22}$$

$$q_{elec} = g_e \exp\left(\frac{D_e}{kT}\right) \tag{2.23}$$

where m is the molecular mass, V is the total volume of the ideal gas, Λ is the de Broglie wavelength of the ideal gas particle; g_e and D_e are the degeneracy of the energy state and the reference minimum potential for the electronic partition function q_{elec}, respectively; θ_l and N_v are the characteristic vibrational temperature and number of vibrational degrees of freedom of the particle, respectively; and I and σ_s are the moment of inertia and the symmetry number of the ideal gas molecule representing the number of indistinguishable orientations of the molecule, respectively.

Since the total energy of the molecule can be written as the sum of translational, vibrational, rotational and electronic energies, the overall partition function, Q can be written as the product of individual partition functions [19, 20]:

$$Q = q_{trans}\, q_{vib}\, q_{rot}\, q_{elec} \tag{2.24}$$

Thus, the chemical potential and specific enthalpy can be evaluated as [16, 19]

$$\frac{\mu_{id}}{kT} = -\left(\frac{\partial \ln Q}{\partial N}\right)_{V,T} = -\ln\left[\left(\frac{m}{2\pi\hbar^2}\right)^{3/2} \frac{(kT)^{5/2}}{P}\right] - \ln\left(q_{vib}\, q_{rot}\, q_{elec}\right) \tag{2.25}$$

and

$$\frac{h_{id}}{kT} = T\left(\frac{\partial \ln Q}{\partial T}\right)_{V,N} + \frac{Pv}{kT} = 4 - \frac{D_e}{kT} + \sum_{l=1}^{3} \frac{\theta_l}{2T} + \sum_{l=1}^{3} \frac{\theta_l/T}{\exp\left(\theta_l/T\right) - 1} \tag{2.26}$$

where v is the molecular volume, and the subscript $'id'$ indicates that the expressions are valid only when ideal gas assumptions are appropriate.

2.3.2 Incompressible liquid treatment

The liquid phase is considered to be incompressible and an expression for its chemical potential can be found in terms of a reference state. If the saturation condition is chosen as its reference state, then

$$\mu^{\alpha}(T^{\alpha}, P^{\alpha}) = \mu[T^{\alpha}, P_{\infty}(T^{\alpha})] + v_{\infty}^{\alpha}[P^{\alpha} - P_{\infty}(T^{\alpha})] \tag{2.27}$$

where v_{∞}^{α} is the specific volume of the saturated liquid. The saturated state is also approximated as an ideal gas (just like the vapor phase) and its chemical potential is described by Equation 2.25.

Applying classical kinetic theory for the equilibrium state, the equilibrium exchange rate is determined as the rate at which molecules from the vapor phase collide with the liquid-vapor interface assuming that all vapor molecules that collide with the interface successfully transfer to the liquid phase. Thus, at equilibrium conditions, the equilibrium exchange rate can be written as [3, 16]:

$$K_e = \frac{P_e}{\sqrt{2\pi m k T_e}} \tag{2.28}$$

where P_e and T_e are the equilibrium pressure and temperature of the system.

2.3.3 Ideal SRT expression

Substituting Equations 2.25 to 2.28 in Equation 2.19, the evaporation rate is evaluated in terms of known thermodynamic quantities as [16, 17]:

$$J = \frac{P_e^\beta}{\sqrt{2\pi m k T^\alpha}} \left(\exp\left(\frac{\Delta S}{k}\right) - \exp\left(\frac{-\Delta S}{k}\right) \right) \tag{2.29}$$

where

$$\begin{aligned} \frac{\Delta S}{k} = \ln\left[\left(\frac{T^\beta}{T^\alpha}\right)^4 \frac{P_\infty(T^\alpha)}{P^\beta}\right] + \ln\left(\frac{q_{vib}(T^\beta)}{q_{vib}(T^\alpha)}\right) + \frac{v_\infty}{kT^\alpha}(P^\alpha - P_\infty(T^\alpha)) \\ + \left(\frac{1}{T^\beta} - \frac{1}{T^\alpha}\right) \sum_{l=1}^{3} \left(\frac{\theta_l}{2} + \frac{\theta_l}{\exp\left(\theta_l/T^\beta\right) - 1}\right) + 4\left(1 - \frac{T^\beta}{T^\alpha}\right) \end{aligned} \tag{2.30}$$

and where P_e^β is the vapor phase pressure when the liquid-vapor system is in equilibrium. Since at equilibrium the temperature of the isolated sub-volume (and actually the entire system) will be the temperature of the liquid reservoir, $T^\beta = T^\alpha$, the temperature appearing as T_e in Equation 2.28 will be T^α.

P_e^β can be evaluated by using the fact that chemical potentials of the liquid and vapor phase become equal at equilibrium. The chemical potential of the liquid phase is described by Equation 2.27 and considering the vapor to be an ideal gas, its chemical potential can

be written as

$$\mu^{\beta}(T^{\alpha}, P_e^{\beta}) = \mu[T^{\alpha}, P_{\infty}(T^{\alpha})] + kT^{\alpha} \ln\left(\frac{P_e^{\beta}}{P_{\infty}}\right) \tag{2.31}$$

Equating Equation 2.31 to Equation 2.27, P_e^{β} is written as

$$P_e^{\beta} = P_{\infty}(T^{\alpha}) \exp\left(\frac{v_{\infty}^{\alpha}}{kT^{\alpha}}[P_e^{\alpha} - P_{\infty}(T^{\alpha})]\right) \tag{2.32}$$

In the experiments conducted and analyzed by Ward and Fang [1, 16, 17], evaporation flux was measured for different pressures in the vapor phase. The liquid temperature was fixed and the pressure in the liquid phase was determined by the Laplace equation:

$$P^{\alpha} = P^{\beta} + \frac{2\gamma}{R_c} \tag{2.33}$$

where γ is the interfacial tension and R_c is the measured interface curvature. Thus, using Equation 2.33 in Equations 2.30 and 2.32, the dependence of evaporation flux on liquid pressure is removed and so Equations 2.29 and 2.30, which are now in terms of experimentally measurable, or otherwise known, quantities only, can be used to predict vapor pressure for a particular flux to compare with the measured value of vapor pressure [16, 17].

2.4 Statistical Rate Theory - Nonideal corrections

Until now, Statistical Rate Theory for evaporation has only been implemented using ideal approximations. Ward and Fang [16, 17] showed that Equation 2.29 with Equation 2.30 is in good agreement with the experimental results for water and octane when evaluated at pressures below 1 kPa and temperatures below room temperature. However, deviations from the experimental results are expected if this expression is used for high temperatures and high pressures where ideal gas approximations are no longer valid. The nonideality of gases at high temperatures and pressures can be quite significant. The objective of this chapter is to develop an expression for the Statistical Rate Theory evaporation rate allowing for nonideality using equations of state.

2.4.1 Departure functions for chemical potential and enthalpy

For an equation of state,

$$Pv = ZkT \tag{2.34}$$

with dimensionless compressibility $Z = Z(T, \rho)$, where ρ is the molar density, departure functions for chemical potential and enthalpy can be derived by taking the difference between the real fluid and the ideal gas property and integrating from the infinite volume condition (where the real fluid and the ideal gas are the same) to the actual volume of the system. Chemical potential and enthalpy departures can be written as [21]:

$$\frac{\mu - \mu_{id}}{kT} = \int_0^\rho \frac{(Z-1)}{\rho} d\rho + (Z-1) - \ln Z \tag{2.35}$$

$$\frac{h - h_{id}}{kT} = \int_0^{\rho} -T\left(\frac{\partial Z}{\partial T}\right)_{\rho} \frac{d\rho}{\rho} + Z - 1 \tag{2.36}$$

Adding Equations 2.35 and 2.36 appropriately to Equations 2.25 and 2.26, the real enthalpy per molecule and chemical potential expressions is obtained based on the equation of state being obeyed in the range of temperature and pressure being considered. If the equation of state is valid for both vapor and liquid phases in this temperature and pressure range, then these chemical potential and enthalpy relations can be used for both the phases.

2.4.2 Nonideal corrections to the equilibrium molecular exchange rate

The equilibrium exchange rate, K_e, is the rate at which molecules from the vapor phase collide with the liquid vapor interface when the system is in equilibrium. To evaluate K_e in terms of equilibrium thermodynamic variables, there is a need to develop an expression for the number of molecules which collide with the interface at given thermodynamic conditions.

Consider a very large hypothetical box of volume V containing N molecules. Consider a hypothetical surface, S (area A) somewhere deep in the interior of the box. The objective is to find the number of molecules crossing the surface S per unit time. Next, consider a differential element dx (big enough to assume a number density N/V), at a distance x from the surface S in the negative x-direction, as shown in Figure 2.2. In one second, only those molecules will strike or cross the surface S, which have a velocity $v_x \geq x$. In a non-rarified gas, the molecules may collide with one another before striking the surface S. Since half of these molecule-molecule collisions will enhance the surface collisions, and half will reduce the surface collisions, without loss of generality, the impact of molecule-

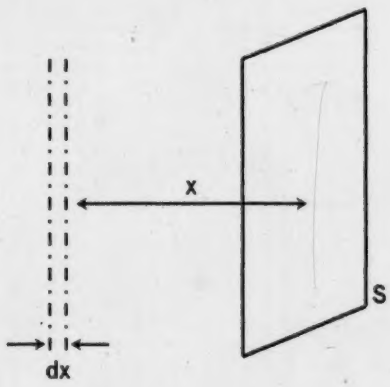

Figure 2.2: Schematic diagram of a hypothetical surface.

molecule collisions can be neglected. Considering a Maxwell-Boltzmann distribution of velocities, the probability of observing a molecule with a velocity v_x is given as [22]

$$p(v_x) = \sqrt{\frac{m}{2\pi kT}} \exp\left[\frac{-mv_x^2}{2kT}\right] \tag{2.37}$$

and so the probability of $v_x \geq x$ is equal to

$$p(v_x \geq x) = \int_x^\infty \sqrt{\frac{m}{2\pi kT}} \exp\left[\frac{-mv_x^2}{2kT}\right] dv_x \tag{2.38}$$

Considering the number density and the volume of the differential element, the total number of molecules in this differential element which may strike or cross the surface S

can be written as

$$K_e^{dV} = \frac{N}{V}(A\,dx)p(v_x \geq x) \tag{2.39}$$

Substituting Equation 2.38 into Equation 2.39, and integrating over all possible distances from the surface, A, the total number of molecules striking or passing through the surface S per unit area per unit time is obtained as:

$$K_e = \int_0^\infty \int_x^\infty \frac{N}{V}\sqrt{\frac{m}{2\pi kT}}\exp\left[\frac{-mv_x^2}{2kT}\right] dv_x dx \tag{2.40}$$

Changing the order of integration (and appropriately adjusting the limits of integration), the above expression can be rewritten as:

$$K_e = \int_0^\infty \int_0^{v_x} \frac{N}{V}\sqrt{\frac{m}{2\pi kT}}\exp\left[\frac{-mv_x^2}{2kT}\right] dx dv_x \tag{2.41}$$

Performing the integration,

$$K_e = \frac{N}{V}\sqrt{\frac{kT}{2\pi m}} \tag{2.42}$$

which is a well known result [16, 17] but it should be noted that it is equally valid for the nonideal case. Considering a general equation of state, N/V can be replaced with P/ZkT from Equation 2.34 to get the final expression for K_e in terms of pressure and temperature as

$$K_e = \frac{1}{Z_e}\frac{P_e}{\sqrt{2\pi mkT_e}} \tag{2.43}$$

Thus, the equilibrium molecular exchange rate is obtained in terms of equilibrium temperature, pressure and compressibility of the gas, the latter of which can be evaluated for a particular equation of state.

Since Equation 2.43 was derived for a Maxwell-Boltzmann distribution in the gas, Z_e will be the compressibility of the gas phase ($Z^\beta(P_e^\beta, T_e^\beta)$) and as before $T_e = T^\alpha$. Therefore, expression 2.19 can be evaluated for high temperatures and pressures by using the nonideal corrections to chemical potential (Equation 2.35), enthalpy (Equation 2.36) and the equilibrium exchange rate (Equation 2.43) in Equation 2.19 to yield:

$$J = \frac{1}{Z_e^\beta} \frac{P_e^\beta}{\sqrt{2\pi m k T^\alpha}} \left(\exp \frac{\Delta S}{k} - \exp \frac{-\Delta S}{k} \right) \tag{2.44}$$

where

$$\begin{aligned} \frac{\Delta S}{k} = & \ln \left[\left(\frac{T^\beta}{T^\alpha} \right)^4 \frac{P_\infty(T^\alpha)}{P^\beta} \right] + \ln \left(\frac{q_{vib}(T^\beta)}{q_{vib}(T^\alpha)} \right) + \frac{v_\infty}{kT^\alpha} (P^\alpha - P_\infty(T^\alpha)) \\ & + \left(\frac{1}{T^\beta} - \frac{1}{T^\alpha} \right) \sum_{l=1}^{3} \left(\frac{\theta_l}{2} + \frac{\theta_l}{\exp(\theta_l / T^\beta) - 1} \right) + 4 \left(1 - \frac{T^\beta}{T^\alpha} \right) + \\ & \left[\int_0^{\rho^\alpha} \frac{(Z^\alpha - 1)}{\rho^\alpha} d\rho^\alpha + (Z^\alpha - 1) - \ln Z^\alpha \right] \\ & - \left[\int_0^{\rho^\beta} \frac{(Z^\beta - 1)}{\rho^\beta} d\rho^\beta + (Z^\beta - 1) - \ln Z^\beta \right] \\ & + \left[\int_0^{\rho^\beta} -T^\beta \left(\frac{\partial Z^\beta}{\partial T^\beta} \right)_{\rho^\beta} \frac{d\rho^\beta}{\rho^\beta} + Z^\beta - 1 \right] \left(1 - \frac{T^\beta}{T^\alpha} \right) \end{aligned} \tag{2.45}$$

2.4.3 An example - The Peng-Robinson equation of state

Since most hydrocarbons are well described using the Peng-Robinson equation of state, the Peng-Robinson equation of state is taken as an example to predict evaporation rates for hydrocarbons. The Peng-Robinson equation of state is given by [23]

$$P = \frac{RT}{\overline{v} - b} - \frac{a\alpha}{\overline{v}^2 + 2b\overline{v} - b^2} \tag{2.46}$$

$$a = \frac{0.45724 R^2 T_c^2}{P_c}$$

$$b = \frac{0.07780 R T_c}{P_c}$$

$$\alpha = \left(1 + \left(0.37464 + 1.54226\omega - 0.26992\omega^2\right)\left(1 - T_r^{0.5}\right)\right)^2$$

where $\overline{v}$ is the molar volume, ω is the acentric factor and T_r is the reduced temperature, $T_r = \frac{T}{T_c}$. In terms of compressibility defined by Equation 2.34, Equation 2.46 can be rearranged to give [24]

$$Z^3 - (1 - B)Z^2 + (A - 3B^2 - 2B)Z - (AB - B^2 - B^3) = 0 \tag{2.47}$$

where $A = \frac{a\alpha P}{R^2T^2}$ and $B = \frac{bP}{RT}$. The integrals in Equations 2.35 and 2.36 can be evaluated for the Peng-Robinson equation of state to give [25]:

$$\frac{\mu - \mu_{id}}{kT} = \left[Z - 1 - \ln(Z - B) - \frac{A}{B\sqrt{8}} \ln\left(\frac{Z + (1+\sqrt{2})\, B}{Z + (1-\sqrt{2})\, B} \right) \right] \tag{2.48}$$

$$\frac{h - h_{id}}{kT} = \left[Z - 1 - \left(\frac{A}{B\sqrt{8}} - \frac{a_c\,(d\alpha/dT)}{bR\sqrt{8}} \right) \ln\left(\frac{Z + (1+\sqrt{2})\, B}{Z + (1-\sqrt{2})\, B} \right) \right] \tag{2.49}$$

Thus, our final expression for the evaporation flux according to the Peng-Robinson equation of state is:

$$J = \frac{1}{Z_e^{\beta}} \frac{P_e^{\beta}}{\sqrt{2\pi m k T^{\alpha}}} \left(\exp\left(\frac{\Delta S}{k} \right) - \exp\left(\frac{-\Delta S}{k} \right) \right) \tag{2.50}$$

where

$$\begin{aligned}\frac{\Delta S}{k} = &\ln\left[\left(\frac{T^\beta}{T^\alpha}\right)^4 \frac{P_\infty(T^\alpha)}{P^\beta}\right] + \ln\left(\frac{q_{vib}(T^\beta)}{q_{vib}(T^\alpha)}\right) + \frac{v_\infty}{kT^\alpha}(P^\alpha - P_\infty(T^\alpha)) \\ &+ \left(\frac{1}{T^\beta} - \frac{1}{T^\alpha}\right)\sum_{l=1}^{3}\left(\frac{\theta_l}{2} + \frac{\theta_l}{\exp\left(\theta_l/T^\beta\right) - 1}\right) + 4\left(1 - \frac{T^\beta}{T^\alpha}\right) + \\ &\left[Z^\alpha - 1 - \ln\left(Z^\alpha - B^\alpha\right) - \frac{A^\alpha}{B^\alpha\sqrt{8}}\ln\left(\frac{Z^\alpha + \left(1+\sqrt{2}\right)B^\alpha}{Z^\alpha + \left(1-\sqrt{2}\right)B^\alpha}\right)\right] \\ &- \left[Z^\beta - 1 - \ln\left(Z^\beta - B^\beta\right) - \frac{A^\beta}{B^\beta\sqrt{8}}\ln\left(\frac{Z^\beta + \left(1+\sqrt{2}\right)B^\beta}{Z^\beta + \left(1-\sqrt{2}\right)B^\beta}\right)\right] \\ &+ \left[Z^\beta - 1 - \left(\frac{A^\beta}{B^\beta\sqrt{8}} - \frac{a_c\left(d\alpha/dT\right)}{bR\sqrt{8}}\right)\ln\left(\frac{Z^\beta + \left(1+\sqrt{2}\right)B^\beta}{Z^\beta + \left(1-\sqrt{2}\right)B^\beta}\right)\right]\left(1 - \frac{T^\beta}{T^\alpha}\right)\end{aligned} \tag{2.51}$$

P_e^β can be evaluated by using the fact that chemical potentials of the liquid and vapor phase become equal at equilibrium ($\mu^\alpha(T^\alpha, P_e^\alpha) = \mu^\beta(T^\alpha, P_e^\beta)$). These chemical potentials can be obtained using the Peng-Robinson equation of state for both the phases to evaluate P_e^β. However, this adds computational complexity to the iterative calculation of equilibrium vapor pressure that corresponds to a particular evaporation flux. Therefore, Equation 2.32 is used again to evaluate P_e^β, while the compressibility of the vapor phase and the saturation pressure (which appears in Equation 2.32) used, is evaluated using the Peng-Robinson equation of state. It must be noted that the need to evaluate P_e^β as different from the saturation pressure arises only because of the curvature of the interface but Equations 2.50 and 2.51 are equally valid for flat interfaces. In the case of flat interfaces, P_e^β is equal to the saturation pressure at the liquid temperature and can be evaluated using the Peng-Robinson equation of state.

Since the characteristic temperatures of vibration which appear in the vibrational partition function are not available for hydrocarbons, both the ideal SRT and Peng-

Robinson based SRT expression are evaluated neglecting the vibrational terms in the final rate expressions.

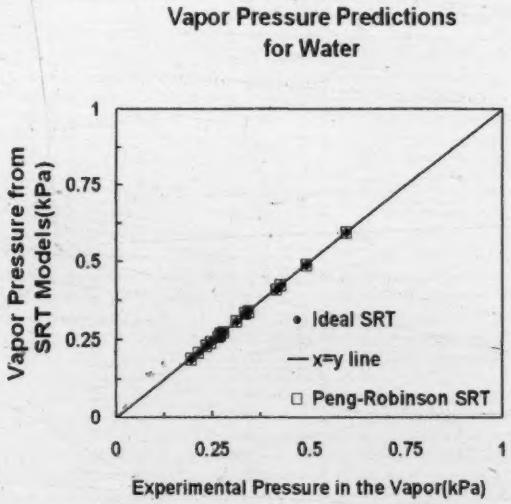

Figure 2.3: Using the experimentally measured values of the radius of curvature and the temperatures on both sides of the interface for water (from Tables I and II in Ref. [16]), vapor pressures have been predicted using the ideal [16] and the Peng-Robinson based SRT model that would result in the experimentally measured evaporation flux. The predicted values of the vapor pressure for both models have been plotted on the ordinate, against the experimentally measured vapor pressure values on the abscissa. The points will lie on the 45^o line, if they are in perfect agreement.

2.5 Results

2.5.1 Comparison with previous experiments

As was indicated during the sensitivity analysis in Refs. [16] and [17], SRT calculations should be done to predict the vapor pressure for a particular evaporation flux rather than predicting evaporation rates for a particular vapor pressure. This is done because it was noted that evaporation flux can be predicted accurately only if the vapor pressure of hydrocarbons is measured to within 0.002 Pa (an un-achievable accuracy). During the evaluation, the liquid-vapor interface was assumed to be spherical, resulting in a pressure difference (liquid pressure higher than the vapor pressure) of $2\gamma/R_c$, where γ is the interfacial tension and R_c is the radius of curvature.

As is evident from Figure 2.3, measurements and predictions based on both the ideal and the Peng-Robinson based SRT model, are in excellent agreement with each other for evaporation of water at low pressures (below 1 kPa) and temperatures (below room temperature). At such experimental conditions, the nonideal additional terms in the Peng-Robinson based SRT model (Equation 2.50 with Equation 2.51) are negligible. Measurements and predictions for octane (shown in Figure 2.4) are also observed to be in close agreement and again predictions based on the ideal model are very close to the predictions based on the Peng-Robinson based SRT model.

2.5.2 Further predictions based on Peng-Robinson SRT

In order to identify the range where fluid nonidealities become significant and where the Peng-Robinson based SRT model would yield better results than the ideal SRT model,

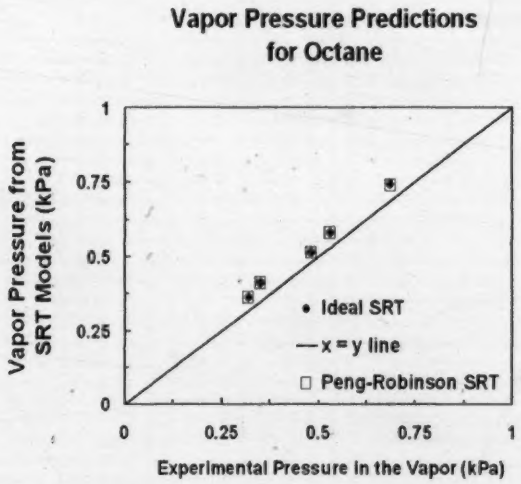

Figure 2.4: Using the experimentally measured values of the radius of curvature and the temperatures on both sides of the interface for octane (from Table I in Ref. [17]), vapor pressures have been predicted using the ideal [17] and the Peng-Robinson based SRT model that would result in the experimentally measured evaporation flux. The predicted values of the vapor pressure for both models have been plotted on the ordinate, against the experimentally measured vapor pressure values on the abscissa. The points will lie on the 45^o line, if they are in perfect agreement.

predictions are made for the evaporation flux at temperatures near the critical temperatures. Ethane ($T_c = 32.28^oC$) and butane ($T_c = 152.05^oC$) have been chosen because their critical temperature values are low compared to other hydrocarbons and so experiments could be done easily.

As was indicated in Refs. [1], [16] and [17], the temperature jump across the interface decreases with an increase in the vapor pressure, it can be concluded that the temperature jump across the interface can be neglected while predicting evaporation flux at very high

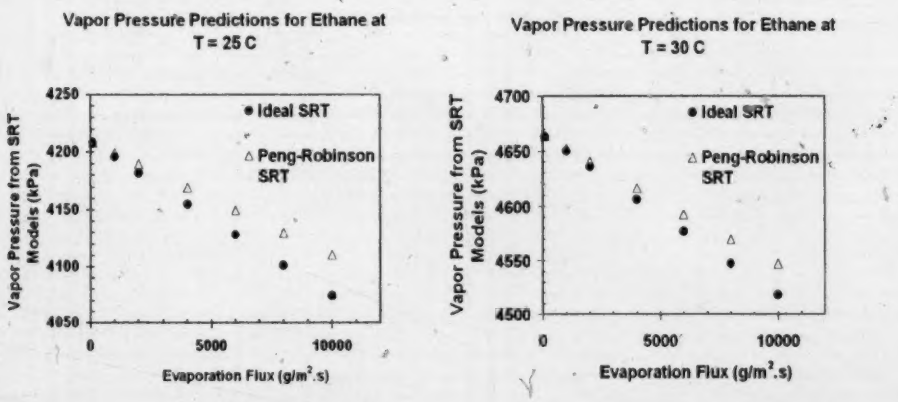

Figure 2.5: Predictions for ethane at $T = 25^oC$ and $T = 30^oC$ made using both the ideal and the Peng-Robinson based SRT model after assuming a zero temperature jump at the interface, have been shown. The predicted values of the vapor pressure for both the models have been plotted on the ordinate, against the evaporation flux on the abscissa. Deviations can be seen for high flux values.

pressures and temperatures (in the near-critical region). Since the liquid vapor surface almost disappears, the surface tension is low and there is not much of a pressure difference; however, the pressure difference was still taken to be $2\gamma/R_c$ with a value of $R_c = 5\,mm$ for all the calculations. Surface tension values were taken from Hysis (v3.1, Hyprotech Ltd.) (ethane: $\gamma = 0.12406\,dyne/cm$ at 30^oC, $0.51307\,dyne/cm$ at 25^oC, butane: $\gamma = 1.6548\,dyne/cm$ at $400K$)). Predictions were made at two different temperatures, $T = 25^oC$ and $T = 30^oC$ for ethane with both the ideal and the Peng-Robinson based SRT models. The vapor pressure predictions from both the models have been plotted against evaporation flux in Figure 2.5. It can be observed that the vapor pressure decreases (almost linearly) with the evaporation flux, and the deviation between the predictions from both the models increases with evaporation flux.

Similar results were also obtained for butane at 400 K and the vapor pressure pre-

dictions have been plotted against the evaporation flux in Figure 2.6. In all cases it was found that the Peng-Robinson based SRT model predicted a higher vapor pressure than the ideal SRT model for the same evaporation flux.

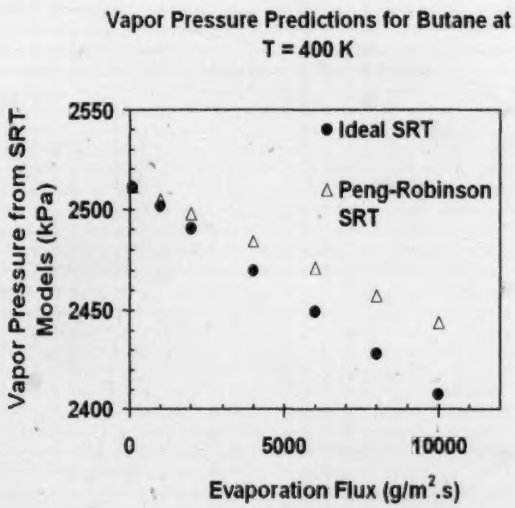

Figure 2.6: Predictions for butane at $T = 400K$ made using both the ideal and the Peng-Robinson based SRT models after assuming a zero temperature jump at the interface, have been shown. The predicted values of the vapor pressure for both the models have been plotted on the ordinate, against the evaporation flux on the abscissa. Deviations can be seen for high flux values.

As there is no way to *'a priori'* predict the temperature jump (it was a measured quantity in Refs. [1], [16] and [17]), and as the temperature jump was found to decrease with the evaporation flux, no temperature jump was assumed in the above calculations. Further, a sensitivity analysis of the evaporation flux with the temperature jump across the interface was done by assuming a temperature difference of 2 K for butane, with the vapor side temperature higher than the liquid side temperature and the results are shown in Figure 2.7. It can be inferred that a minor temperature difference across the interface

does not affect the predictions on vapor pressures and so, plots of vapor pressures vs. evaporation flux would look similar to the plots for zero temperature jumps. Thus, a minor temperature difference across the interface would make no significant difference in the predictions, or our conclusions.

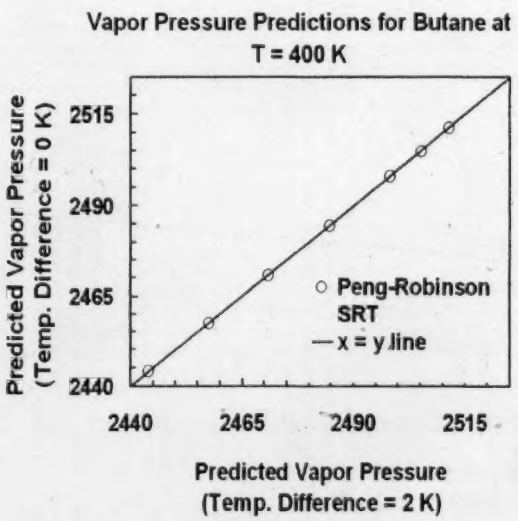

Figure 2.7: The Peng-Robinson based SRT model was used to predict the vapor pressure for a liquid temperature of $400K$ for butane assuming temperature jumps of 0 and $2K$ across the interface. The predicted values of the vapor pressure for zero temperature difference across the interface are plotted on the ordinate, against the predicted vapor pressure values for a temperature jump of $2K$ across the interface, on the abscissa. If they were in perfect agreement, they lie on the 45^o line.

2.6 Conclusions

A Statistical Rate Theory formulation incorporating fluid nonidealities using equations of state was presented to develop a generic equation-of-state based SRT model for liquid evaporation. The Peng-Robinson equation-of-state based SRT model was found to predict evaporation rates as accurately as the ideal SRT model at low temperatures (below room temperature) and pressures (below 1 kPa) and was found to differ from the ideal model at sufficiently higher temperatures and pressures (near the critical temperature). The Peng-Robinson based SRT model predicted higher vapor pressures than the ideal SRT model irrespective of the temperature jump across the interface. Experiments should be done in the near-critical region (temperatures higher than $0.8T_c$) to investigate the predictions that have been made.

References

[1] Fang, G.; Ward, C. A. *Physical Review E*, **1999**, 59(1), 417.

[2] Schrage, R. W. In *A Theoretical Study of Interphase Mass Transfer;* Columbia University Press: New York, 1953, Chap. 3.

[3] Ward, C. A.; Findlay, R. D.; Rizk, M. *J. Chem. Phys.*, **1982**, 76(11), 5599.

[4] Elliott, J. A. W.; Ward, C. A. In *Equilibria and Dynamics of Gas Adsorption on Heterogenous Solid Surfaces;*, Elsevier: Amsterdam, **1997**, 104, 285.

[5] Ward, C. A.; Elliott, J. A. W. *Applied Surface Science*, **2002**, 196, 202.

[6] Ward, C. A.; Rizk, M.; Tucker, A. S. *J. Chem. Phys.*, **1982**, 76, 5606.

[7] Ward, C. A.; Findlay, R. D. *J. Chem. Phys.*, **1982**, 76, 5615.

REFERENCES

[8] Findlay, R. D.; Ward, C. A. *J. Chem. Phys.*, **1982**, 76, 5624.

[9] Elliott, J. A. W.; Ward, C. A. *J. Chem. Phys.*, **1997**, 106(13), 5667.

[10] Elliott, J. A. W.; Ward, C. A. *J. Chem. Phys.*, **1997**, 106(13), 5677.

[11] Ward, C. A.; *J. Chem. Phys.*, **1983**, 79(11), 5605.

[12] Torri, M.; Elliott, J. A. W. *J. Chem. Phys.*, **1999**, 111(4), 1686.

[13] Dejmek, M.; Ward, C. A. *J. Chem. Phys.*, **1998**, 108, 8698.

[14] Skinner, F. K.; Ward, C. A.; Bardakjian, B. L. *BioPhys. J.* **1993**, 65, 618.

[15] Elliott, J. A. W.; Elmoazzen, H. Y.; McGann, L. E. *J. Chem. Phys.*, **2000**, 113(16), 6573.

[16] Ward, C. A.; Fang, G. *Physical Review E*, **1999**, 59(1), 429.

[17] Fang, G.; Ward, C. A. *Physical Review E*, **1999**, 59(1), 441.

[18] Callen, H. B. In *Thermodynamics and an Introduction to Thermostatics;* 2nd Ed., John Wiley and Sons, Inc., 1985; Chap. 3.

REFERENCES

[19] Hill, T. L. In *An Introduction to Statistical Thermodynamics;* Dover: New York, 1986; p. 74-80.

[20] McQuarrie, D. A. In *Statistical Mechanics;* University Science Books, 2003; p. 85-107.

[21] Elliott, J. R.; Lira, C. T. In *Introductory Chemical Engineering Thermodynamics;* Prentice Hall, 1999, p. 235.

[22] Bird, R. B.; Stewart, W. E.; Lightfoot, E. N. In *Transport Phenomena;* 2^{nd} Ed., John Wiley and Sons, Inc., 2002, p. 38.

[23] Peng, D. Y.; Robinson, D. B. *Industrial and Engineering Chemistry: Fundamentals,* **1976**, 15, 58.

[24] Elliott, J. R.; Lira, C. T. In *Introductory Chemical Engineering Thermodynamics;* Prentice Hall, 1999, p. 203.

[25] Elliott, J. R.; Lira, C. T. In *Introductory Chemical Engineering Thermodynamics;* Prentice Hall, 1999, p. 240-241.

Chapter 3

Lattice Boltzmann simulations for asymptotic incompressible flow profiles with a periodic pressure gradient [1]

3.1 Introduction

The oscillating flow of an incompressible viscous fluid in long channels has been investigated in detail for different geometries both experimentally and analytically. Pulsating viscous flow of an incompressible fluid due to an oscillating pressure gradient in a long

[1] This chapter has been submitted with slight modifications for publication authored by A. Kapoor and Phillip Y.K. Choi.

channel with a circular cross section has been considered experimentally by Richardson and Tyler [1]. They also conducted experiments for a long channel with a square cross-section and discovered annular effects in the flow. Analytical solutions for laminar, developed, oscillating flows between parallel [2] impermeable plates due to an applied oscillating pressure gradient have been reported in literature. Wang [3] treated pulsating flow in a porous channel between parallel plates theoretically. Tsangaris and Vlachakis [4] derived the analytical solution for pulsating flow in a rectangular duct with porous walls with a constant cross-sectional velocity. Sexl [5] treated the oscillating flow in a circular cross-section theoretically to get annular effects in the flow as discovered experimentally by Richardson and Tyler [1]. Uchida [6] analyzed pulsating viscous flow superposed on the steady laminar motion of incompressible fluid in a circular pipe.

Dean [7] and Goldstein [8] studied the laminar steady flow in a cylindrical annulus, due to a constant circumferentially acting pressure gradient using the narrow gap and finite gap approximations. Tsangaris and Vlachakis [9] analyzed the pulsating flow in a cylindrical annulus using the finite gap approximation. Khamrui [10] solved the Navier-Stokes equations for the fully developed laminar oscillating flow in a long channel with elliptic cross-section. Tsangaris and Vlachakis [11] derived the exact solution of the Navier-Stokes equations for the oscillating flow in a duct with a cross-section of a right-angled isosceles triangle. Drake [12] considered the oscillating flow due to an applied periodic pressure gradient in a rectangular duct and derived asymptotic forms of velocity and stress (skin-friction) which are valid for high frequencies. There is a conspicuous lack of information on how the stress behaves as the frequency of oscillation is changed. This information is very necessary for stress analysis of systems where periodic flows are involved including arterial flow of blood during hypertension conditions (artery wall rupture analysis) and blood flow in kidney-dialysis bags. The scope of this study is to numerically compute the oscillating flow characteristics in a channel of rectangular cross-section and follow the trends in the velocity and stress profiles as frequency is increased from low to moderate and high frequencies. A Lattice Boltzmann equation model has been used to simulate the incompressible pulsating flow in a long channel with a rectangular section due to an

imposed oscillating pressure gradient.

The Lattice Boltzmann (LB) method has been used as a relatively new and promising method for simulating viscous fluid flows for over a decade now. In recent years, there has been a significant advancement in the application of this technique to complex problems including turbulent single-phase flows, multi-phase flows like particle suspensions in fluid, and multi-component flows like in porous media. Lattice Boltzmann models are found to be at least as robust, stable, accurate and computationally efficient as other traditional methods of computation. In the last decade, various LB models have been applied successfully to hydrodynamic problems where traditional computational methods like finite difference or finite element method yield inaccurate results including problems like crystallization [13], magnetohydrodynamics [14, 15], and chemically reactive flows [16].

In this chapter, a 3-D Lattice Boltzmann model is used to simulate the pulsating flows in a rectangular duct due to low, moderate and high periodic pressure gradients and the results are compared with the analytical solutions of Drake [12]. The rest of the chapter is organized as follows: In Section 3.2, the LB method used for the simulation is introduced, followed by the computational issues with LB models in section 3.3. The analytical solution of oscillating flows in a rectangular duct is presented in Section 3.4. In Section 3.5, the numerical simulation results for low and high frequencies for velocity and stress is presented. Finally, in Section 3.6 concluding remarks are presented.

3.2 The Lattice Boltzmann equation - A review

3.2.1 The Boltzmann equation

Historically, the Lattice Boltzmann (LB) equation model was first developed empirically from its predecessor, the lattice gas automaton (LGA), but unlike LGA and other molecular dynamics (MD) approaches, the LB method follows the time evolution of a discrete particle-velocity distribution function instead of tracking single particles. Theoretically, the Boltzmann equation can be derived from classical statistical mechanics, considering its evolution from the Liouville equation. The Liouville equation is the most fundamental equation of classical statistical mechanics. In a classical dynamical state of a system of N particles, 6N variables (3N momentum, p_i and 3N spatial coordinates, r_j) are required to completely describe one point in a phase space. However, one never knows all these 6N coordinates in a macroscopic system but a few macroscopic properties of the system, such as energy, pressure, mean velocity, density etc. are known. Since there are an enormously large number of points in phase space which are compatible with these few known macroscopic quantities, a phase space density or a distribution function, f_N is defined as the fraction of phase points in the volume $dr_1 dr_2 ... dp_{3N}$ i.e. the fraction of phase points which corresponds to a state of the system where particle 1 is spatially in between $r_1.r_2, r_3$ and $r_1 + dr_1, r_2 + dr_2, r_3 + dr_3$ and has a momentum in between p_1, p_2, p_3 and $p_1 + dp_1, p_2 + dp_2, p_3 + dp_3$, and so on for other particles. The Liouville equation (Equation 3.1) is the equation of motion that this phase space distribution function must satisfy during its trajectory in time and is equivalent to the 6N Hamilton equations of motion for the N-particle system.

$$\frac{\partial f_N}{\partial t} + \sum_{j=1}^{N} \frac{\mathbf{p}_j}{m_j} \cdot \nabla_{\mathbf{r}_j} f_N \; + \sum_{j=1}^{N} \mathbf{F}_j \cdot \nabla_{\mathbf{p}_j} f_N = 0 \tag{3.1}$$

where m_j is the mass of j^{th} particle, $\nabla_{\mathbf{r}_j}$ and $\nabla_{\mathbf{p}_j}$ denote the gradient with respect to the spatial and momentum variables respectively in f_N; and $\mathbf{F}_j$ is the net force on the j^{th} particle. On introduction of reduced distribution functions in the Liouville equation [17], the BBGKY (Bogoliubov, Born, Green, Kirkwood, Yvon) hierarchy can be derived as

$$\frac{\partial f^{(n)}}{\partial t} + \sum_{j=1}^{n} \frac{\mathbf{p}_j}{m_j} \cdot \nabla_{\mathbf{r}_j} f^{(n)} + \sum_{j=1}^{n} \mathbf{X}_j \cdot \nabla_{\mathbf{p}_j} f^{(n)} + \sum_{i,j=1}^{n} \mathbf{F}_{ij} \cdot \nabla_{\mathbf{p}_j} f^{(n)} + \sum_{j=1}^{n} \int \int \mathbf{F}_{j,n+1} \cdot \nabla_{\mathbf{p}_j} f^{(n+1)} d\mathbf{r}_{n+1} d\mathbf{p}_{n+1} = 0 \tag{3.2}$$

where $f^{(n)}$ is the n^{th} reduced distribution function given as

$$f_N^{(n)}(\mathbf{r}_1, \mathbf{r}_2, ..., \mathbf{r}_n, \mathbf{p}_1, ..., \mathbf{p}_n, t) = \frac{N!}{(N-n)!} \int ... \int f_N(\mathbf{r}_1, ..., \mathbf{p}_N, t) \, d\mathbf{r}_{n+1} ... d\mathbf{r}_N d\mathbf{p}_{n+1} ... d\mathbf{p}_N$$

Reduced distribution functions are defined because for all general purposes of interest, only $f^{(1)}$ and $f^{(2)}$ are necessary as they represent the two-body and three-body interactions respectively. The BBGKY (Equation 3.2) hierarchy is applicable to systems with any density. However, the major problem in the application of this equation is the coupling of a distribution function with the next higher order distribution function. No successful method to decouple the BBGKY hierarchy has yet been devised. For systems where a dilute gas approximation can be made, molecules interact weakly with other molecules and hence only two-body interactions are important. Thus, only $f^{(1)}$, the singlet distribution function is relevant. This singlet distribution function, also called the particle-velocity distribution function encompasses all the statistical information related to the position and momentum of the particles in the system. Boltzmann derived an equation for f

(superscript (1) dropped from here on), using collision theory as:

$$\frac{\partial f_j}{\partial t} + \mathbf{v}_j \cdot \nabla_{\mathbf{r}} f_j + \frac{1}{m_j}\mathbf{X}_j \cdot \nabla_{\mathbf{v}_j} f_j = 2\pi \sum_i \int\int \{f_i' f_j' - f_i f_j\} g_{ij} b \, db \, d\mathbf{v}_i \tag{3.3}$$

where subscripts i and j represent the two molecules which approach each other for a collision, primes denote their post-collisional distribution functions and the right hand side collision term takes into account all molecules lost or entered into the position range $(\mathbf{r},\ \mathbf{r}+d\mathbf{r})$ and the velocity range $(\mathbf{v},\ \mathbf{v}+d\mathbf{v})$ by summing over all possible collisions of molecule j.

Equation 3.3, the Boltzmann equation, is the fundamental equation of the rigorous kinetic theory of gases. This is a non-linear integrodifferential equation and thus solving it is very complicated even for simple systems. Various models have been proposed to approximate the right-hand side integral expression (collision term) in Equation 3.3 in order to solve the Boltzmann equation for fluid-mechanical systems.

3.2.2 The Lattice Boltzmann equation

Due to the integral right hand side term in the Boltzmann equation, it is very complex to discretize the equation and solve it for fluid flow phenomena. Various LB models have been proposed to approximate the collision term in terms of deviation variables from equilibrium. Among these different LB models, the BGK (Bhatnagar, Gross, Krook) model [18] with a single relaxation time approximation is the most widely accepted model as it assumes that the main effect of the collision term is to bring the particle-velocity

distribution function closer to the equilibrium distribution.

$$\partial_t f + \xi.\nabla f = -\frac{1}{\lambda}[f - f^{(eq)}] \tag{3.4}$$

where $f^{(eq)}$ is the Maxwell-Boltzmann equilibrium distribution function, λ is the relaxation time due to collision and ξ is the velocity space vector.

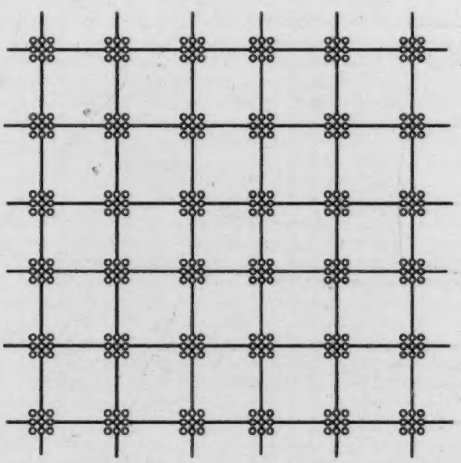

Figure 3.1: Schematic of a typical 2-dimensional 9-discrete lattice velocity (D2Q9) lattice in a 2D Lattice Boltzmann calculation. Each lattice node contains 9 cells, each of which stores a particle distribution function corresponding to the particular lattice velocity assigned to the cell.

A general lattice for a LB calculation thus looks like the schematic shown in Figure 3.1. Although, there is a probability for particles to achieve any velocity in the range $(-\infty, +\infty)$ and in any direction, for computational purposes, only certain velocity directions are allowed. Hence, Equation 3.4 can be discretized in velocity space [19, 20] by

using a set of velocities resulting in the discrete velocity model of the LBGK Equation as:

$$\partial_t f_\alpha + \xi_\alpha . \nabla f_\alpha = -\frac{1}{\lambda}[f_\alpha - f_\alpha^{(eq)}] \tag{3.5}$$

where f_α is the distribution function corresponding to the αth discrete velocity ξ_α and $f_\alpha^{(eq)}$ is the corresponding equilibrium function. Depending on the dimensionality of the problem, various models have been proposed to discretize the velocity space. The most popular ones are, D2Q9 for 2-D flows and D3Q15 or D3Q19 [21] (Figure 3.2) for three-dimensional (3-D) flows. Equation 3.5 can further be discretized in space and time such that $\delta x = \mathbf{e}_\alpha \delta t$ is always the displacement vector from the lattice site to its neighboring sites.

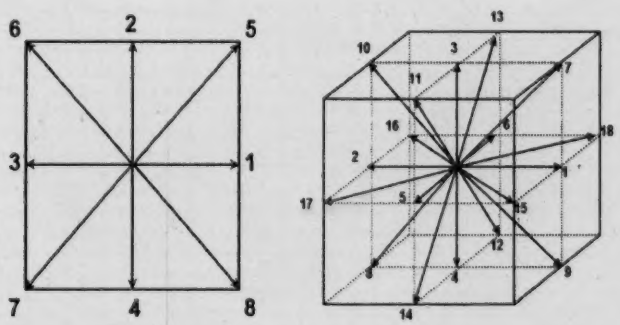

Figure 3.2: Lattice velocities of the D2Q9 (left) and D3Q19 (right) models.

$$f_\alpha\left(\mathbf{x}_i + \mathbf{e}_\alpha \delta t, t + \delta t\right) - f_\alpha(\mathbf{x}_i, t) = -\frac{1}{\tau}\left[f_\alpha(\mathbf{x}_i, t) - f_\alpha^{(eq)}(\mathbf{x}_i, t)\right] \tag{3.6}$$

where $\tau = \lambda/\delta t$ is the non-dimensional relaxation time. The equilibrium distribution

function can be obtained using a Taylor series expansion of velocity up to second order and can be expressed as [21]:

$$f_\alpha^{eq} = w_\alpha \rho[1 + \frac{3}{c^2}(\mathbf{e}_\alpha.\mathbf{u}) + \frac{9}{2c^4}(\mathbf{e}_\alpha.\mathbf{u})^2 - \frac{3}{2c^2}\mathbf{u}^2] \tag{3.7}$$

where ρ is the local density of the node, $\mathbf{e}_\alpha$ is the lattice velocity, $c = \delta x/\delta t$ and w_α is the weighting factor (for D3Q19) given by

$$w_\alpha = \begin{cases} 1/3 & \alpha = 0, \\ 1/18 & \alpha = 1 \text{ to } 6, \\ 1/36 & \alpha = 7 \text{ to } 18. \end{cases}$$

The pressure is given by $p = \rho c_s^2$ (ideal gas equation of state) where the speed of sound is given by $c_s = c/\sqrt{3}$ [21] and $\nu = (2\tau - 1)/6$, is the kinematic viscosity.

For D3Q19, the lattice velocities are defined as :

$$\vec{\mathbf{e}_\alpha} = \begin{cases} 0 & \alpha = 0, \\ (\pm 1, 0, 0), (0, \pm 1, 0), (0, 0, \pm 1) & \alpha = 1 \text{ to } 6, \\ (\pm 1, \pm 1, 0), (\pm 1, 0, \pm 1), (0, \pm 1, \pm 1) & \alpha = 7 \text{ to } 18 \end{cases} \tag{3.8}$$

The density and momentum fluxes can be evaluated in terms of the distribution func-

tion by considering the moment integration of the distribution functions as

$$\rho = \sum_{\alpha=0}^{N} f_\alpha = \sum_{\alpha=0}^{N} f_\alpha^{eq} \quad \text{and} \tag{3.9}$$

$$\rho \mathbf{u} = \sum_{\alpha=0}^{N} f_\alpha \mathbf{e}_\alpha = \sum_{\alpha=0}^{N} f_\alpha^{eq} \mathbf{e}_\alpha \tag{3.10}$$

The Chapman-Enskog expansion [22] can be employed to obtain the Navier-Stokes equations from the LB equation. It is a multi-scale expansion [23] with rescaling of time and space as

$$\begin{aligned} t_1 = \epsilon t, \quad t_2 = \epsilon^2 t, \quad x_1 = \epsilon x, \\ \frac{\partial}{\partial t} = \epsilon \frac{\partial}{\partial t_1} + \epsilon^2 \frac{\partial}{\partial t_2}, \quad \frac{\partial}{\partial x} = \epsilon \frac{\partial}{\partial x_1} \end{aligned} \tag{3.11}$$

The particle-velocity distribution function in Equation 3.6 can be expanded as

$$f_\alpha = f_\alpha^{(0)} + \epsilon f_\alpha^{(1)} + \epsilon^2 f_\alpha^{(2)} + \boldsymbol{O}(\epsilon^3) \tag{3.12}$$

to recover the Navier-Stokes equations in the incompressible limit as [21]

$$\rho\left[\frac{\partial \mathbf{u}}{\partial t} + (\mathbf{u}\cdot\nabla)\mathbf{u}\right] = \rho\mathbf{F} + \mu\nabla^2\mathbf{u} \tag{3.13}$$

with $\rho\mathbf{F} = -\nabla P$.

3.3 Computational issues

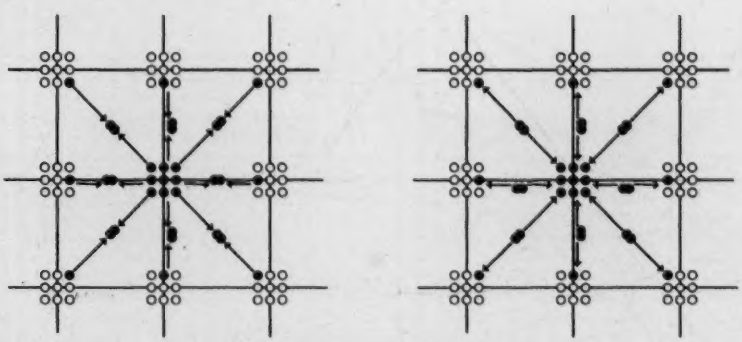

Figure 3.3: A schematic showing the collision time step (left) followed by a streaming time step (right) in a D2Q9 lattice model. Black (left) and red (right) color nodes represent that the pre-collision and post-collision values of the distribution function respectively.

Computationally, Equation 3.6 is applied in two steps, a relaxation (collision) time step and a streaming time step [24]:

The relaxation (collision) time step (as shown in Figure 3.3) is described by:

$$\tilde{f}_\alpha(\mathbf{x}_i, t+\delta t) = f_\alpha(\mathbf{x}_i, t) - \frac{1}{\tau}[f_\alpha(\mathbf{x}_i, t) - f_\alpha^{(eq)}(\mathbf{x}_i, t)] \tag{3.14}$$

and the streaming time step by:

$$f_\alpha(\mathbf{x}_i + \mathbf{e}_\alpha \delta t, t+\delta t) = \tilde{f}_\alpha(\mathbf{x}_i, t+\delta t) \tag{3.15}$$

where $\tilde{f}_\alpha$ is the post collision distribution function. This two-step division makes the solution procedure explicit, easy to implement and parallelize. This also helps saving computational space and time as, in the relaxation time step, post-collision distribution function values overwrite the pre-collision values and then in the streaming step get streamed to their next lattice points.

3.3.1 Boundary conditions

In a typical LB flow computation, two kinds of boundaries are encountered: a solid wall boundary and an open boundary. The no-slip boundary condition is applied at the solid wall while periodic conditions are applied at the open boundaries. Open boundaries include lines of symmetry, inlets and outlets, where macroscopic variables like velocity and pressure are known instead of the particle distribution function. However, periodic boundary conditions can be employed at these open boundaries without ambiguity. However, at solid walls, the no-slip boundary condition (zero fluid velocity at stationary walls),

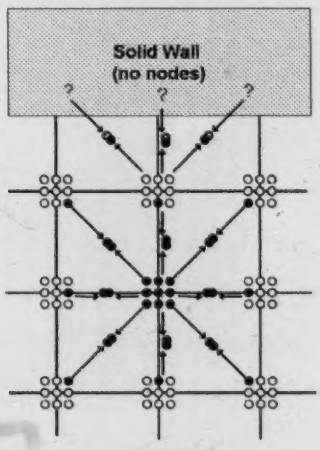

Figure 3.4: A schematic showing the importance of boundary conditions for the D2Q9 model. For near-wall nodes, the collision step is incomplete as there are no fluid nodes in the wall and so post-collision distribution function values can not be updated for the near-wall nodes.

can only be satisfied approximately through solving f_α's. The problem, also shown in Figure 3.4, is that right after the collision step, there are no f_α's which can stream from the wall to the lattice node right next to the walls. Various models have been proposed to approximate these f_α's. A popular implementation of the no-slip boundary condition is to employ the bounce-back scheme [25, 26] in which the momentum of the incoming particle is exactly reversed in the opposite direction by the collision with the wall. Various improvements to this scheme have also been proposed. Zou and He [27] proposed an extension of the bounce-back scheme considering the reversal of the non-equilibrium part of the distribution function only. Inamuro et al. [28] used a counter-slip velocity to nullify the slip effects induced by the bounce-back scheme. Ladd [29, 30] showed that if the wall is placed exactly in the middle of the lattice nodes, the bounce back scheme is second order accurate in predicting zero velocity at the wall.

3.3.2 Force evaluation

Stress evaluation in a fluid-flow problem is crucial to the study of fluid mechanics. Various stress evaluation techniques including surface stress integration [31, 32] and the momentum exchange method [33, 29, 30] have been proposed. He and Doolen [34] used the stress integration approach to evaluate the stress on a cylinder in the flow field by integrating the stress on the surface. This integration involves accurate computation of $\nabla \mathbf{u}$. Since $\mathbf{u}$ is not the primary variable in the simulation, evaluating $\nabla \mathbf{u}$ degrades the accuracy. Ladd [30] proposed the momentum exchange method using the bounce back boundary condition by considering the momentum exchange of the particles with the wall per unit time. Since this scheme is based on the simple bounce back scheme, it is also second-order accurate if applied to cases where the wall is placed in the middle of the lattice nodes.

3.4 Pulsating flow in a duct - The problem

Incompressible flow in a long cylindrical channel due to a periodic pressure gradient has been studied experimentally by Richardson and Tyler [1]. They also conducted experiments for the flow in a channel with a square duct cross section. Drake [12] considered the incompressible flow in a long channel of rectangular cross-section due to a periodic pressure gradient theoretically by solving the Navier-Stokes equation. This section reviews the analytical series solution obtained by Drake for the oscillating flow in a 3-D duct. Consider an incompressible flow in a rectangular duct driven by a periodic pressure gradient as shown in Figure 3.5.

The governing equation of incompressible flow driven by a periodic pressure gradient is:

$$\frac{\partial v_x}{\partial t} = K\cos\omega t + \nu\left(\frac{\partial^2 v_x}{\partial y^2} + \frac{\partial^2 v_x}{\partial z^2}\right) \tag{3.16}$$

with

$$v_x(y,z) = 0; y = \pm a$$
$$v_x(y,z) = 0; z = \pm b$$

where $\partial P/\partial x = Re[-K\rho\exp(i\omega t)]$ is the periodic pressure gradient in the direction of the flow and ν is the kinematic viscosity. Using separation of variables, the periodic velocity can be obtained as a series solution:

$$v_x(y,z,t) = Re[F(y,z).\exp(i\omega t)]$$

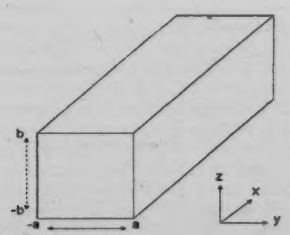

Figure 3.5: Schematic of a rectangular duct across which a pulsating pressure drop is applied.

where

$$F(y,z) = \frac{4Kb^2}{\pi\nu}\sum_{n=0}^{\infty}\frac{(-1)^n}{(2n+1)p^2}\left(1-\frac{\cosh(py/a)}{\cosh(pa/b)}\right)\times\cos\left(\frac{(2n+1)}{2b}\pi z\right) \tag{3.17}$$

with $p = \left(\frac{i\omega b^2}{\nu} + \frac{(2n+1)^2}{4}\pi^2\right)^{\frac{1}{2}}$

The solution behaves differently for different frequencies of oscillation of the periodic pressure gradient. At low frequencies, the solution behaves as a quasi-steady one, while at higher frequencies, complex phenomena in the velocity flow profiles are seen.

3.5 Results

In the LB simulation, a simple geometry of a square duct is considered to be meshed into a resolution of 60 (flow direction) x 20 x 20. A periodic pressure gradient ($\Delta P/\Delta x$) of $-0.01\cos\omega t$ (in lattice units) is applied across the channel. It is applied as a density difference among the lattice nodes in the flow direction. The average density of the fluid is chosen to be 1.5 (in lattice units) and $\omega = \frac{2\pi}{T_p}$ is the frequency of oscillation and T_p represents the time period of the oscillation of the periodic pressure gradient. T_p is varied from 1536 to 48 time periods to study the effect of frequency of oscillation on the flow phenomena.

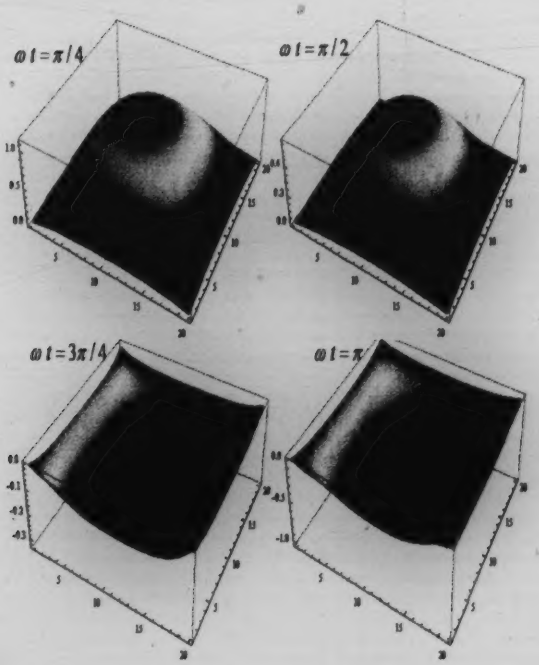

Figure 3.6: 3-D cross-sectional (resolution 20 x 20) velocity profiles at four different times for low frequency velocity solution with 1536 time steps. The velocity profile is of parabolic type and the centre-most point achieves the maximum amplitude during a period.

3.5.1 Low frequency flow

For low values of $\omega b^2/\nu$ (also called Womersley Number [35]), the solution can be obtained as [12]

$$v_x(y,z,t) = \frac{16Kb^2}{\pi^3\nu}\sum_{n=0}^{\infty}\frac{(-1)^n}{(2n+1)^3}\left(1-\frac{\cosh\frac{(2n+1)}{2b}\pi y}{\cosh\frac{(2n+1)}{2b}\pi a}\right)\times\cos\left(\frac{(2n+1)}{2b}\pi z\right)\cos\omega t \quad (3.18)$$

The variation of the velocity profile with time looks very similar to the applied pressure gradient. It can be seen that there is no phase lag between the velocity of the fluid and the pressure gradient and at any particular time, the velocity solution behaves as that for a steady pressure gradient, $-K\rho\cos\omega t$.

Figure 3.6 shows the streamline velocity (normalized by the maximum velocity during the period) at four different times during the period for $T_p = 1536$. It can be seen that the velocity profile is of parabolic type and the centreline velocity is larger than velocity near the walls of the duct at all times. The velocity profile seems to be in phase with the applied pressure gradient and a minor phase lag of 0.17π was noted. It can be inferred that for small values of frequency, the flow behaves as a quasi-steady one. As the frequency of pressure oscillation is increased further, the flow becomes more complicated and the phase lag between the velocity and the applied pressure gradient keeps increasing and annular effects begin to develop.

To study moderate frequency flows a time period of 576 time steps was chosen. Figure 3.7 (right) shows the streamline velocity (normalized by the maximum velocity during the period) at four different times during the period for $T_p = 576$. It can be seen that unlike the low frequency case, the streamline velocity gets more complex as the annular effects start building up. For most of the time during the period, the velocity profile imitates the applied pressure gradient in terms of having a parabolic profile; however, at around $\omega t = 3\pi/4$, it can be see that the velocity near the walls is almost constant with a high velocity region in the core. This happens right after the pressure difference across the channel becomes zero and the pressure reversal starts (back pressure becomes higher than the front pressure). Observing the plot ($\omega t = 3\pi/4$) for points close to the wall, it can be seen that some minor dips in the velocity start building up due to the pressure reversal. As the frequency is increased further, these regions increase and the velocity distribution starts exhibiting Stokes layer character with high velocity gradients at the wall. The velocity increases in the direction of the applied pressure gradient sharply near the solid boundaries and then decreases to zero again, leaving the core which oscillates in

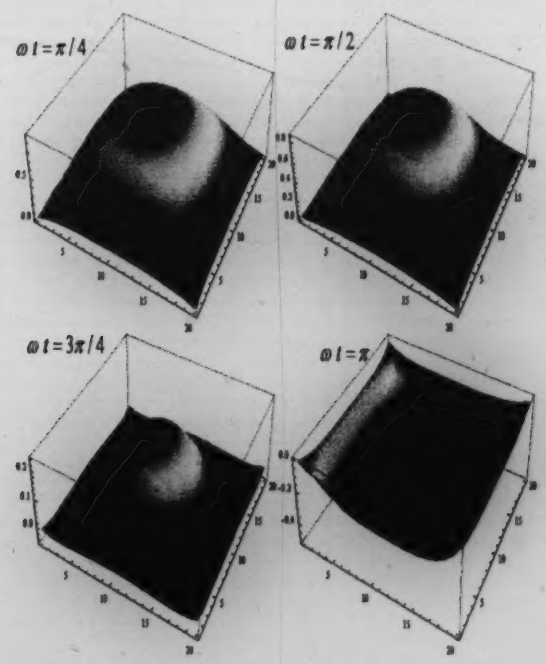

Figure 3.7: 3-D cross-sectional (resolution 20 x 20) velocity profiles at four different times for low frequency velocity solution with 576 time steps. The development of annular effects [12] can be seen in the second quadrant and the velocity profile starts exhibiting a Stokesian nature.

direction opposite to that of the applied pressure gradient. Figure 3.8 shows the phase lag between the centreline velocity and the applied pressure gradient. It can be seen that the phase lag has increased from 0.17π ($T_p = 1536$) to 0.35π ($T_p = 576$). Also, unlike the case of low frequency flows, different regions have different phase lags due to annular effects.

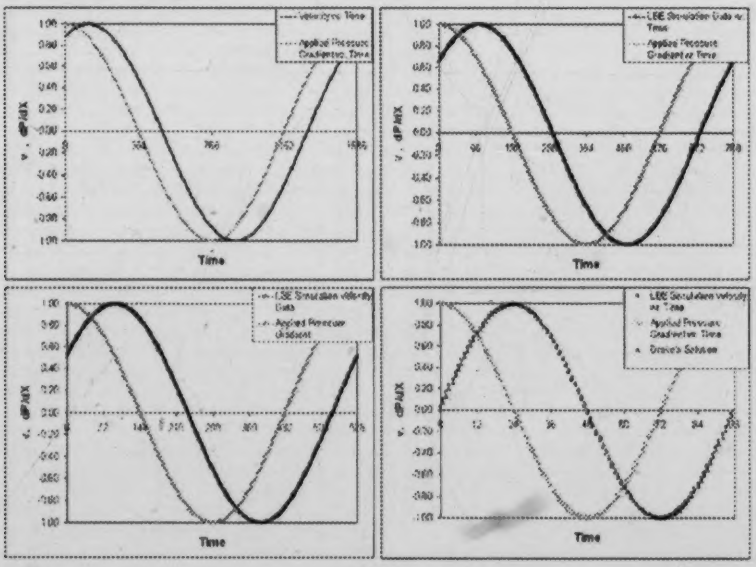

Figure 3.8: Phase difference between velocity and pressure gradient for *Top Left:* Low frequency (1536 timesteps, phase difference: 0.17π), *Top Right:* Moderate frequency (768 timesteps, phase difference: 0.28π), *Bottom Left:* High frequency (576 timesteps, phase difference: 0.35π) and *Bottom Right:* Very High frequency (96 timesteps, phase difference: 0.5π).

3.5.2 High frequency flow

Asymptotic forms for velocity were obtained by Drake for higher frequencies by employing integral representations to sum the infinite series in the solution (Equation 3.17) obtained from the method of separation of variables. Different regions in the duct have different forms of velocity profiles and thus a different phase lag from the pressure gradient. Considering the symmetry of the duct, two expressions are required, one for the midpoint of the wall ($z \sim 0, y \sim a$ or $y \sim 0, z \sim b$) and the other for the center of the duct. This leaves the

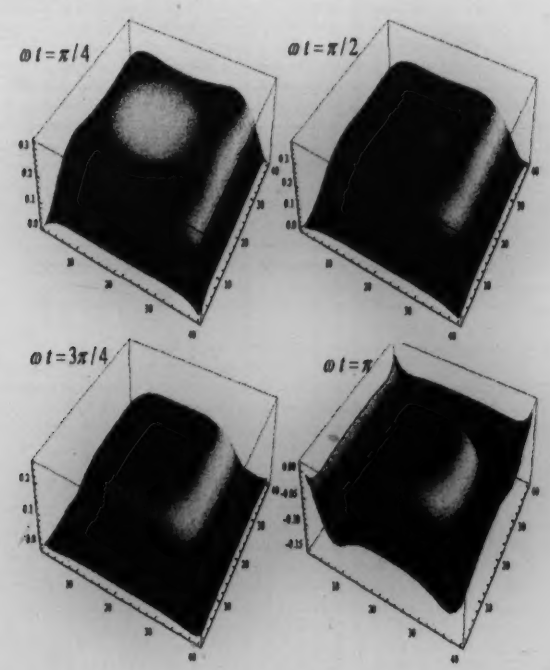

Figure 3.9: 3-D cross-sectional velocity profiles at four different times for high frequency velocity solution with 96 time steps. Annular effects and flattening effects are significant and the centre-most point no longer achieves the maximum velocity amolitude.

region in the corner of the duct where the solution is quite complicated. This is expected because near the corner the boundary layers of the adjacent walls coalesce. However, this region diminishes in size as a and b increase. The asymptotic form of the velocity profile for the mid-wall where $\omega(b-z)^2/\nu$ and $\omega y^2/\nu$ are large, has been approximated by Drake [12] as:

$$v_x \sim Re\left\{\frac{K}{i\omega}\left(1-\exp(-\lambda(a-y))-\exp(-\lambda(b-z))erf\left[\frac{\lambda^{\frac{1}{2}}(a-y)}{2^{\frac{1}{2}}(b-z)^{\frac{1}{2}}}\right]\right)\exp(i\omega t)\right\} \quad (3.19)$$

where $\lambda = (i\omega/\nu)^{\frac{1}{2}}$.

At the center of the channel (regions of small y and small z), it can be easily shown from Equation 3.17 that velocity can be approximated as $\frac{K}{\omega}\sin\omega t$. Thus the centreline velocity lags behind the pressure gradient by a phase angle of $\pi/2$.

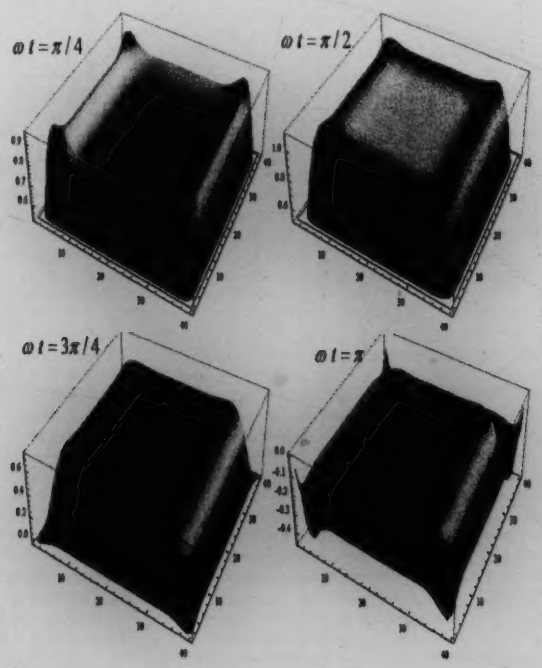

Figure 3.10: 3-D cross-sectional (resolution: 40 x 40) velocity profiles at four different times for high frequency velocity solution with 48 time steps. Annular effects and flattening effects are significant and sharp velocity gradients develop near the wall.

Two time periods, 96 and 48 time steps, were chosen to study highly oscillating flows. Figures 3.9 and 3.10 show the streamline velocity (normalized by the maximum velocity during the period) at four different times during the period for $T_p = 96$ and $T_p = 48$ respectively. The resolution of the channel was increased to 60 x 40 x 40 to increase the

Womersley number and to check for any effects that may be caused because of the mesh-size. However, the solution was found to be similar with the increased resolution and it can be concluded that a resolution of 20 x 20 is almost as good as 40 x 40 resolution. It can be seen that for $T_p = 96$ (left) at $\omega t = \pi/4$, the centerline velocity is less than the velocity at points near it. The parabolic profile of low and moderate frequency flow is lost and the velocity profiles develop sharply near the wall (Stokes layer character) and stay constant (flat profile, as in inviscid flows) elsewhere in the duct. It can be inferred that the boundary layer does not diffuse much and the central region of the channel behaves as inviscid approaching the velocity profile of the inviscid oscillating flow. Figure 3.10 shows that at $\omega t = \pi/4$ for $T_p = 48$ time steps, velocity near the walls is higher than the velocity in the center and as time increases during the period, the velocity amplitude of the fluid in the core of the duct is quite reduced as compared to low frequency cases. Figure 3.8 shows that the phase lag between the velocity and the pressure gradient has reached its asymptotic value of $\pi/2$ for high frequency flows. This is in accordance to Drake's approximation of centreline velocity as $(\frac{K}{\omega}\sin\omega t)$ for high frequency flows. The phase angle (lag) near the walls approaches a constant value of $\pi/4$. These Stokesian velocity characteristics, also known as 'annular effects' are reported by Richardson and Tyler [1] experimentally.

3.5.3 Stress at high frequencies

Asymptotic velocity expressions (Equation 3.19) can further be employed to obtain expressions for the skin friction valid for points near the center of the wall of the duct. Drake derived the skin friction ($\tau_{z=b}$) on the wall as the sum of integrals which can be approximated for points near the center of the wall as

$$\tau_{z=b} \sim K\rho\left(\frac{\nu}{\omega}\right)^{\frac{1}{2}}\cos\left(\omega t - \frac{\pi}{4}\right) \tag{3.20}$$

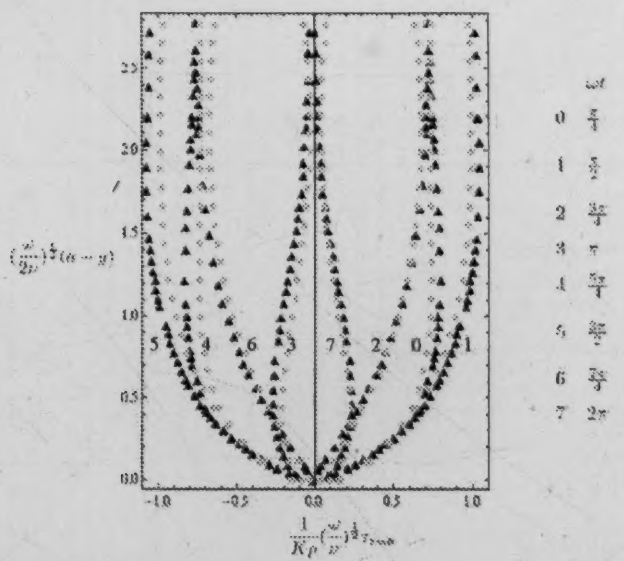

Figure 3.11: Normalized stress from the analytical solution (light points) by Drake [12] and from the LB simulation (dark triangles) have been plotted on the abscissa against the normalized distance on the ordinate. As is evident from the plot, that the LB simulation results are in close agreement with the analytical solution.

Thus, stress at the center of the wall has a phase lag of $\pi/4$ behind the pressure gradient.

Drake's integrals for skin friction at points away from the center of the wall can be evaluated numerically. The numerical solution has been plotted as $\frac{1}{K\rho}(\frac{\omega}{\nu})^{\frac{1}{2}}\tau_{z=b}$ against $(\frac{\omega}{2\nu})^{\frac{1}{2}}(a-y)$ in Figure 3.11. LB simulation stress results (calculated from the momentum exchange method [33, 29, 30]) have also been plotted and it can be seen that the results are concordant. It can be seen that as y tends to a, i.e. on approaching near the corner of the duct, $\tau_{z=b}$ becomes 0. Also except for $\omega t = \pi/2,\ 3\pi/2$, $\partial\tau_{z=b}/\partial y$ is infinite at the corner. This is in agreement with the analytical solution for stress. Stress at the midpoint

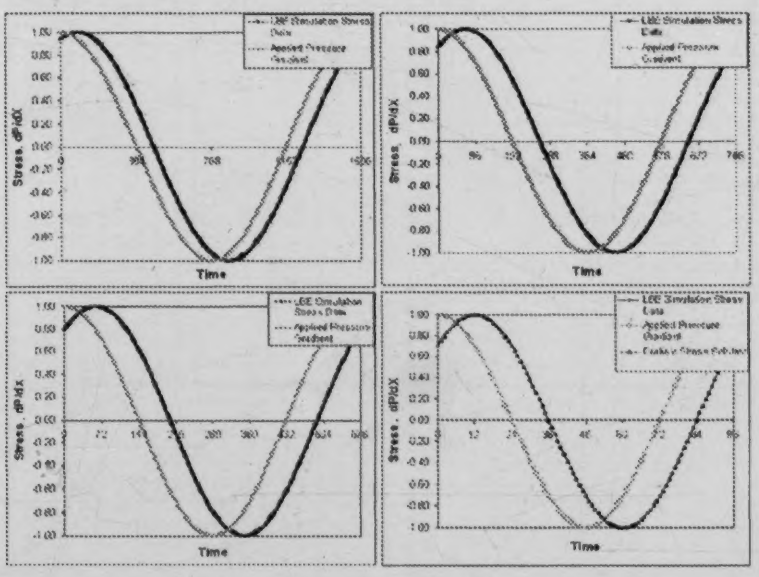

Figure 3.12: Phase difference between stress and pressure gradient for *Top Left:* Low frequency (1536 timesteps, phase difference: 0.13π), *Top Right:* Moderate frequency (768 timesteps, phase difference: 0.19π), *Bottom Left:* High frequency (576 timesteps, phase difference: 0.22π) and *Bottom Right:* Very High frequency (96 timesteps, phase difference: 0.25π).

of the wall ($y \sim 0, z \sim b$) was evaluated for different frequencies and has been plotted in Figure 3.12. It can be seen that the phase lag between stress and pressure gradient increases from 0.13π for $T_p = 1536$ to $\pi/4$ for $T_p = 96$. Increasing the frequency further to 48 time periods does not affect the phase lag and it can be said that the phase lag has reached an asymptotic value of $\pi/4$. This is in accordance with Drake's approximation of stress (Eq. 19). This can be explained by the fact that the velocity phase lag near the walls approaches an asymptotic value of $\pi/4$ resulting in a similarly patterned strain phase lag and hence leading to the stress phase asymptotic value of $\pi/4$.

3.6 Conclusions

Pulsating flow in a rectangular duct due to a periodic pressure gradient has been studied using a 3-D Lattice Boltzmann model. For low frequency flows, it is found that the velocity profiles are parabolic in nature and behave as that for a steady pressure gradient with minor phase lags behind the pressure gradient. As the frequency is increased from low to moderate, weak annular effects start building up and velocity profiles start lagging behind the pressure gradient. On further increase of frequency to very high values, annular effects become strong and both the amplitude and the phase angle are affected. The velocity amplitude reduces while the phase angle(lag) increases with the increase in the frequency. The velocity profiles exhibit a Stokes layer character and develop sharply near the wall to a maximum value and then decrease slightly to a value which remains constant for most of the duct. The central region of the duct behaves as an inviscid fluid approaching inviscid oscillating velocity profiles. The velocity phase lag behind the pressure gradient reaches its asymptotic value of $\pi/2$ in the central region and $\pi/4$ near the walls. Stress evaluations were done and the results were found to be in accordance with the analytical solutions. It was noted that like the velocity profiles, stress phase lag behind the applied pressure gradient also reaches an asymptotic value of $\pi/4$. It was also found that stress is maximum in the middle of the duct walls and decreases to zero towards the corners. This will help one in designing and optimizing medical apparatuses and understanding the medical flow phenomena.

References

[1] Richardson, E.G.; Tyler, E. *Proc. Phys. Soc.*, **1929**, 42, 1.

[2] Lamb, H. In *Hydrodynamics;*, Cambridge University Press. **1932**.

[3] Wang, C.Y. *ASME J. Appl. Mech.*, **1971**, 38, 553.

[4] Tsangaris, S.; Vlachakis, N.W. *J. Fluids Eng., Trans. ASME*, **2003**, 125, 382.

[5] Sexl, Th. *Z. Physik*, **1930**, 61, 349.

[6] Uchida, S. *J. Appl. Math. (ZAMP)*, **1956**, 7, 403.

[7] Dean, W.R. *Proc. Roy. Soc. London A*, **1928**, 121, 402.

[8] Goldstein, S. In *Modern Developments in Fluid Dynamics;* Clarendon Press, Oxford. **1938**, 315.

[9] Tsangaris, S.; Vlachakis, N.W. *Applied Mathematical Modelling*, **2007**, 31, 1899.

[10] Khamrui, S.R. *Bull. Cal. Math. Soc.*, **1957**, 49, 57.

[11] Tsangaris, S.; Vlachakis, N.W. *J. Appl. Math. (ZAMP)*, **2003**, 54(6), 1094.

[12] Drake, D.G.*Quart. J. Mech. Appl. Math.*, **1965**, 18(1), 1.

[13] Kang, Q; Zhang, D; Lichtner, P.C.; Tsimpanogiannis, I. N. *Geophysical Research Letters*, **2004**, 31, L21604.

[14] Martinez, D.O.; Chen, S.; Matthaeus, W.H. *Phys. Plasmas* **1994**, 1, 1850.

[15] Dellar, P.J. *J. Comput. Phys.* **2002**, 179, 95.

[16] Manjhi, N.; Verma, N.; Salemb, K.; Mewesb, D. *Chemical Engineering Science* **2006**, 61(8), 2510.

[17] McQuarrie, D. A. In *Statistical Mechanics;* University Science Books, 2003; p. 402-428.

[18] Bhatnagar, PL; Gross, EP; Krook, M. *Phys. Rev.*, **1954**, 94, 511.

[19] He, X; Luo, L.S. *Phys. Rev. E*, **1997**, 55, 6333.

REFERENCES

[20] He, X; Luo, L.S. *Phys. Rev. E*, **1997**, 56, 6811.

[21] Qian, YH; d Humieres, D; Lallemand, P. *Europhys Lett.*, **1992**, 17, 479.

[22] Frisch, U.; d Humieres, D.; Hasslacher, B.; Lallemand, P.; Pomeau, Y; Rivet, J.P. *J. Complex System*, **1987**, 1, 649.

[23] Chapman, S; Cowling, T.G. *Cambridge: Cambridge University Press*, **1970**.

[24] Zanetti, G.; McNamara, G *Phys. Rev. Lett.*, **1988**, 61, 2332.

[25] Ziegler, D.P. *J Stat Phys*, **1993**, 71, 1171.

[26] Ginzbourg, I.; Alder, P.M. *J Phys II France*, **1994**, 4, 191.

[27] Zou, Q.; He, X. Y. *Phys. Fluids*, **1997**, 9, 1591.

[28] Inamuro, T.; Yoshino, M.; Ogino, F. *Phys. Fluids*, **1995**, 7, 2928.

[29] Ladd, A.J.C. *J. Fluid Mech.*, **1994**, 271, 285.

[30] Ladd, A.J.C. *J. Fluid Mech.*, **1994**, 271, 311.

[31] Filippova, O.; Hanel, D. *J. Comput. Phys.*, **1998**, 147, 219.

REFERENCES

[32] He, X.; Zou, Q.; Luo, L.S.; Dembo, M. *J. Comput. Phys.*, **1996**, 129, 357.

[33] Behrend, Q. *Phys. Rev. E*, **1995**, 52, 1164.

[34] He, X.; Doolen, D. *J. Comput. Phys.*, **1997**, 134, 306.

[35] Womersley, J.R. *J. Physiol.*, **1955**, 127, 553.

Chapter 4

Exact solution for circumferentially pulsating annular flow with a constant radial flux [1]

4.1 Introduction

Understanding pulsating flows in a cylindrical annulus with porous walls is fundamentally significant for the design and optimization of various medical apparatuses and for

[1] This work is an obvious extension of the previous work by S. Tsangaris and N. Vlachakis (**"Applied Mathematical Modelling"**, 31(9), p. 1899-1906). However, at the same time when I carried out this research, Tsangaris *et al.* conducted similar research and published it as **"International Journal of Engineering Science"**, 44(20), p. 1498-1509.

understanding biological phenomena. Oscillating flows appear in various medical apparatuses used for fluid delivery and testing like peristaltic pumps, heart-lung machines, and injection-suction therapy equipment.

The Navier-Stokes equations are non-linear partial differential hydrodynamic equations of motion which can only be analytically solved for a few systems. Most of the systems which can be solved analytically, involve laminar or oscillating flows in rectangular channels, in between parallel walls, in cylindrical pipes and pipes with annular cross-sections, both with impermeable and porous walls. Analytical solutions for laminar, fully developed, steady incompressible flow in rectangular channels, with parallel walls, straight ducts with constant cross-section, cylindrical pipes and annular cross-sections date back to the late 19^{th} century.

Pulsating viscous flow of an incompressible fluid due to an oscillating pressure gradient in a long channel with a circular cross section has been considered experimentally by Richardson and Tyler [1]. They also conducted experiments for a long channel with a square cross-section and discovered annular effects in the flow. Analytical solutions for laminar, developed, oscillating flows between parallel [2] impermeable plates due to an applied oscillating pressure gradient have been reported in literature.

Wang [3] treated pulsating flow in a porous channel between parallel plates theoretically. Tsangaris and Vlachakis [4] derived the analytical solution for pulsating flow in a rectangular duct with porous walls with a constant cross-sectional velocity. Sexl [5] treated the oscillating flow in a circular cross-section theoretically to get annular effects in the flow as discovered experimentally by Richardson and Tyler [1]. Uchida [6] analyzed pulsating viscous flow superposed on the steady laminar motion of incompressible fluid in a circular pipe.

Dean [7] first studied the laminar steady flow in a cylindrical annulus due to an applied

circumferential pressure gradient, using the narrow-gap approximation. Goldstein [8] studied the finite gap Dean flow problem. Tsangaris and Vlachakis [9] extended the Dean flow solution to the periodic unsteady solution in a cylindrical annulus with impermeable walls by applying the oscillating, circumferentially acting, pressure gradient. Oscillating flow with solid walls has been studied for various other geometries including parallel plates [2], circular [1, 5, 6, 10], rectangular [11], elliptical [12] and triangular [13] cross-sections. However, in the literature, very few analytical solutions exist for the case of porous walls. An exact solution for steady flow between parallel-porous walls has been studied by Bearman [14] and was extended further for the case of pulsating flow in the parallel-porous channel by C. Y. Wang [3]. Tsangaris and Vlachakis [4] derived the exact solution for the case of an oscillating flow in a rectangular duct with porous walls. However, since most of the mechanical systems involving pulsating flows are cylindrical or annular in nature e.g. flows in medical apparatuses, and cell transport dynamics; there is a need to develop exact solutions of the hydrodynamic equations in cylindrical coordinates. This chapter presents the exact solution of the Navier-Stokes equations for the incompressible flow in a cylindrical annulus with porous walls, when an oscillating circumferential pressure gradient is applied. The rest of the chapter is organized as follows: In section 4.2, the exact analytical solutions of the Navier-Stokes equations is presented for the incompressible flow in an annulus with porous/non-porous walls when an oscillating circumferential pressure gradient is applied. In Section 4.3, results are presented and velocity amplitudes and phase lags are discussed as a function of the oscillating frequency. Finally, a conclusion is given in Section 4.4.

4.2 Method

The present study focusses on solving the hydrodynamic equations of motion for the case of an unsteady, incompressible flow in a cylindrical annulus with porous walls (constant flux case). The Navier-Stokes equations along with the continuity equation have been

written in cylindrical coordinates (r, θ). u_r and u_θ are the radial and the tangential velocity components, respectively. A circumferential oscillating pressure gradient ($\frac{\partial P}{\partial \theta} = -K\rho \exp(i\omega t)$) is imposed on the annulus with injection at radius R_1 (inner wall) and suction at radius R_2 (outer wall). A schematic representation of the problem is shown in Figure 4.1 .

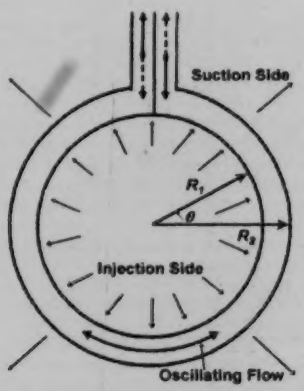

Figure 4.1: Schematic representation of a cylindrical annulus with porous walls (radial flux with injection at the inner wall (R_1) and suction at the outer wall (R_2)) and a circumferentially oscillating pressure gradient across the longitudinal direction.

The steady fully developed Dean Flow solution has been extended to the unsteady solution produced by a periodic pressure gradient assuming a constant flux in the radial direction, thereby satisfying the continuity equation.

$$\frac{1}{r}\frac{\partial (r\, u_r)}{\partial r} = 0 \qquad \Rightarrow \quad u_r = \frac{A}{r} \tag{4.1}$$

Using the fully developed flow condition and the continuity equation, the radial velocity component goes as 1/r, i.e. $u_r = A/r$ and the circumferential velocity component is a

function of the radial coordinate and time only, i.e. $u_\theta = u(r,t)$. The parameter A determines the amount of flux passing through the annulus as $2\pi A = Q$, where Q is the radial volumetric flux per unit length of the annulus. Assume that the spatial and size distribution of the pores in the porous walls does not affect the velocity solution in the flow regime and there is a constant volumetric flux (Q) through the annulus. The radial and the circumferential momentum balance equations can be written as:

$$u_r \frac{\partial u_r}{\partial r} - \frac{u_\theta^2}{r} = -\frac{1}{\rho}\frac{\partial P}{\partial r} - \nu \frac{u_r}{r^2} \tag{4.2}$$

$$\frac{\partial u_\theta}{\partial t} + u_r \frac{\partial u_\theta}{\partial r} + \frac{u_r u_\theta}{r} = -\frac{1}{\rho r}\frac{\partial P}{\partial \theta} + \nu \left[\frac{\partial^2 u_\theta}{\partial r^2} + \frac{1}{r}\frac{\partial u_\theta}{\partial r} - \frac{u_\theta}{r^2} \right] \tag{4.3}$$

The boundary conditions for u_θ result from the no-slip boundary at the inner and the outer walls of the annulus: $u_\theta = 0$ at $r = R_1$ and $r = R_2$ at all times.

4.2.1 Steady flow

Impermeable wall

For steady flow in a cylindrical annulus with impermeable walls, $u_r = 0$ and the circumferential velocity becomes just a function of the radial coordinate, $u_\theta = u_\theta(r)$. Considering

a constant circumferential pressure gradient $\frac{\partial P}{\partial \theta} = -K\rho$, Equation 4.3 can be reduced to

$$\frac{d^2\tilde{u_\theta}}{d\tilde{r}^2} + \frac{1}{\tilde{r}}\frac{d\tilde{u_\theta}}{d\tilde{r}} - \frac{\tilde{u_\theta}}{\tilde{r}^2} + \frac{1}{\tilde{r}} = 0 \tag{4.4}$$

where the following dimensionless variables have been introduced: $\tilde{r} = \frac{r}{R_1}$ and $\tilde{u_\theta} = \frac{u_\theta \nu}{K R_1}$

The solution can be obtained using the no-slip boundary equations at the inner and outer wall of the annulus, which is the same expression as obtained by Goldstein [8]

$$\tilde{u}_\theta = -\frac{1}{2}\tilde{r}\ln\tilde{r} + \frac{1}{2}\ln\lambda\frac{\lambda^2}{\lambda^2-1}\left(\tilde{r} - \frac{1}{\tilde{r}}\right) \tag{4.5}$$

where λ is the ratio of the outer to inner radius of the channel, $\lambda = \frac{R_2}{R_1}$.

Porous wall

For steady flow in a cylindrical annulus with porous walls, $u_r = A/r$ and the circumferential velocity becomes just a function of the radial coordinate, $u_\theta = u_\theta(r)$. Considering a constant circumferential pressure gradient $\frac{\partial P}{\partial \theta} = -K\rho$, Equation 4.3 can be reduced to

$$\frac{d^2\tilde{u_\theta}}{d\tilde{r}^2} + (1-\beta)\frac{1}{\tilde{r}}\frac{d\tilde{u_\theta}}{d\tilde{r}} - (1+\beta)\frac{\tilde{u_\theta}}{\tilde{r}^2} + \frac{1}{\tilde{r}} = 0 \tag{4.6}$$

where the following dimensionless variables have been introduced: $\tilde{r} = \frac{r}{R_1}$, $\beta = \frac{A}{\nu}$, $\tilde{u_\theta} = \frac{u_\theta \nu}{KR_1}$ and $\lambda = R_2/R_1$. The solution can be obtained using the no-slip boundary equations at the inner and outer wall of the annulus as:

$$\tilde{u_\theta} = \frac{\left(\lambda^2 - \tilde{r}^2\right) + \tilde{r}^2\lambda^2\left(\lambda^\beta - \tilde{r}^\beta\right) - \left(\lambda^{2+\beta} - \tilde{r}^{2+\beta}\right)}{2\beta\tilde{r}(\lambda^{2+\beta} - 1)} \tag{4.7}$$

4.2.2 Oscillating flow

Porous wall

Substituting $u_r = \frac{A}{r}$ and $\frac{\partial P}{\partial \theta} = -Re[K\rho\exp(i\omega t)]$ in Equation 4.3,

$$\frac{\partial u_\theta}{\partial t} = \frac{K}{r}e^{i\omega t} + \nu\frac{\partial^2 u_\theta}{\partial r^2} + \frac{(\nu - A)}{r}\frac{\partial u_\theta}{\partial r} - \frac{(\nu + A)}{r^2}u_\theta \tag{4.8}$$

This partial differential equation can be reduced to an ordinary differential equation by employing $u_\theta = V(r)\exp(i\omega t)$ in Equation 4.8 to get

$$\frac{d^2V}{dr^2} + \left(1 - \frac{A}{\nu}\right)\frac{1}{r}\frac{dV}{dr} - \left[\left(1 + \frac{A}{\nu}\right) + \frac{i\omega r^2}{\nu}\right]\frac{V}{r^2} + \frac{K}{\nu r} = 0 \tag{4.9}$$

Introducing the following dimensionless variables, $\tilde{r} = \frac{r}{R_1}$, $\alpha^2 = \frac{\omega R_1^2}{\nu}$, $\beta = \frac{A}{\nu}$, $\tilde{V} = \frac{V\nu}{KR_1}$

and $\lambda = R_2/R_1$, the circumferential momentum equation in the reduced form can be written as:

$$\frac{d^2\tilde{V}}{d\tilde{r}^2} + (1-\beta)\frac{1}{\tilde{r}}\frac{d\tilde{V}}{d\tilde{r}} - \left(1+\beta+i\alpha^2\tilde{r}^2\right)\frac{\tilde{V}}{\tilde{r}^2} + \frac{1}{\tilde{r}} = 0 \tag{4.10}$$

where α is the reduced frequency of oscillation (also called Womersley Number [10]) and β can be considered as the Reynolds number of the flow based on the radial velocity which may significantly affect the flow, if inertial (convection) forces dominate over the viscous forces. Using the substitution,

$$\tilde{V}(\tilde{r}) = \frac{1}{i\alpha^2\tilde{r}} + \tilde{V}_s(\tilde{r}) \tag{4.11}$$

the differential equation can be reduced to

$$\frac{d^2\tilde{V}_s}{d\tilde{r}^2} + (1-\beta)\frac{1}{\tilde{r}}\frac{d\tilde{V}_s}{d\tilde{r}} - \left(1+\beta+i\alpha^2\tilde{r}^2\right)\frac{\tilde{V}_s}{\tilde{r}^2} = 0 \tag{4.12}$$

Making the substitution, $\tilde{V}_h(\tilde{r}) = \tilde{V}_s(\tilde{r}).\tilde{r}^{-\frac{\beta}{2}}$, Equation 4.12 can be reduced to obtain the Bessel differential equation

$$\frac{d^2\tilde{V}_h}{d\tilde{r}^2} + \frac{1}{\tilde{r}}\frac{d\tilde{V}_h}{d\tilde{r}} - \left[i\alpha^2\tilde{r}^2 + \left(1+\frac{\beta}{2}\right)^2\right]\frac{\tilde{V}_h}{\tilde{r}^2} = 0 \tag{4.13}$$

which has the general solution of the form

$$\tilde{V}_h = c_1 J_{\frac{2+\beta}{2}}(-i^{\frac{3}{2}}\alpha\tilde{r}) + c_2 Y_{\frac{2+\beta}{2}}(-i^{\frac{3}{2}}\alpha\tilde{r}) \tag{4.14}$$

where $J_{\frac{2+\beta}{2}}(-i^{\frac{3}{2}}\alpha\tilde{r})$ and $Y_{\frac{2+\beta}{2}}(-i^{\frac{3}{2}}\alpha\tilde{r})$ are Bessel functions of the first and second kinds of $\frac{2+\beta}{2}$ order, respectively and c_1 and c_2 are two constants which will be determined by the boundary conditions: $\tilde{V}(1) = 0$ and $\tilde{V}(\lambda) = 0$.

Substituting $\tilde{V}_h$ back into Equation 4.11 and employing the boundary conditions, the solution for an oscillating flow with porous walls for the constant flux (β treated as a constant with time and position) [2] can be obtained as:

$$\tilde{u}_\theta = Re\left[\left\{\frac{1}{i\alpha^2\tilde{r}} + \tilde{r}^{\frac{\beta}{2}}\left(c_1 J_{\frac{2+\beta}{2}}(-i^{\frac{3}{2}}\alpha\tilde{r}) + c_2 Y_{\frac{2+\beta}{2}}(-i^{\frac{3}{2}}\alpha\tilde{r})\right)\right\}\exp(i\omega t)\right] \tag{4.15}$$

where

$$c_1 = \frac{1}{i\alpha^2}\left[\frac{\lambda^{(\frac{\beta+2}{2})}Y_{\frac{2+\beta}{2}}(-i^{\frac{3}{2}}\alpha) - Y_{\frac{2+\beta}{2}}(-i^{\frac{3}{2}}\alpha\lambda)}{Y_{\frac{2+\beta}{2}}(-i^{\frac{3}{2}}\alpha\lambda)J_{\frac{2+\beta}{2}}(-i^{\frac{3}{2}}\alpha) - Y_{\frac{2+\beta}{2}}(-i^{\frac{3}{2}}\alpha)J_{\frac{2+\beta}{2}}(-i^{\frac{3}{2}}\alpha\lambda)}\right] \tag{4.16}$$

[2] The same solution (in slightly other mathematical form) has also been obtained by S. Tsangaris, D. Kondaxakis and N. Vlachakis who conducted a similar research independently at around the same time and published it in a paper titled *"Exact solution of the Navier-Stokes equations for the pulsating Dean flow in a channel with porous walls"* in the **"International Journal of Engineering Science"**, 44(20), p. 1498-1509.

and

$$c_2 = -\frac{1}{i\alpha^2}\left[\frac{\lambda^{-\left(\frac{3+2}{2}\right)}J_{\frac{2+\beta}{2}}(-i^{\frac{3}{2}}\alpha) - J_{\frac{2+\beta}{2}}(-i^{\frac{3}{2}}\alpha\lambda)}{Y_{\frac{2+\beta}{2}}(-i^{\frac{3}{2}}\alpha\lambda)J_{\frac{2+\beta}{2}}(-i^{\frac{3}{2}}\alpha) - Y_{\frac{2+\beta}{2}}(-i^{\frac{3}{2}}\alpha)J_{\frac{2+\beta}{2}}(-i^{\frac{3}{2}}\alpha\lambda)}\right] \tag{4.17}$$

Impermeable wall

For the case of impermeable walls, the solution can be obtained by putting the radial Reynolds number $\beta = 0$ in the above expression to obtain the unsteady Dean solution. This form is another way of writing the solution obtained by Tsangaris and Vlachakis [9]

$$\tilde{u}_\theta = Re\left[\left\{\frac{1}{i\alpha^2\tilde{r}} + \left(c_1 J_1(-i^{\frac{3}{2}}\alpha\tilde{r}) + c_2 Y_1(-i^{\frac{3}{2}}\alpha\tilde{r})\right)\right\}\exp(i\omega t)\right] \tag{4.18}$$

where

$$c_1 = \frac{1}{i\alpha^2}\left[\frac{\lambda^{-1}Y_1(-i^{\frac{3}{2}}\alpha) - Y_1(-i^{\frac{3}{2}}\alpha\lambda)}{Y_1(-i^{\frac{3}{2}}\alpha\lambda)J_1(-i^{\frac{3}{2}}\alpha) - Y_1(-i^{\frac{3}{2}}\alpha)J_1(-i^{\frac{3}{2}}\alpha\lambda)}\right] \tag{4.19}$$

and

$$c_2 = -\frac{1}{i\alpha^2}\left[\frac{\lambda^{-1}J_1(-i^{\frac{3}{2}}\alpha) - J_1(-i^{\frac{3}{2}}\alpha\lambda)}{Y_1(-i^{\frac{3}{2}}\alpha\lambda)J_1(-i^{\frac{3}{2}}\alpha) - Y_1(-i^{\frac{3}{2}}\alpha)J_1(-i^{\frac{3}{2}}\alpha\lambda)}\right] \tag{4.20}$$

Equation 4.15 is the master solution from which steady, unsteady solutions for both solid and porous walls can be obtained. In the limit $(\alpha, \beta) \to 0$, steady solution (Equation 4.5) for a solid wall case can be obtained. The unsteady-periodic solution (Equation 4.18) for a solid wall case can be obtained in the limit $\beta \to 0$ and the steady solution for porous walls (Equation 4.7) can be obtained in the limit $\alpha \to 0$.

4.3 Results and discussion

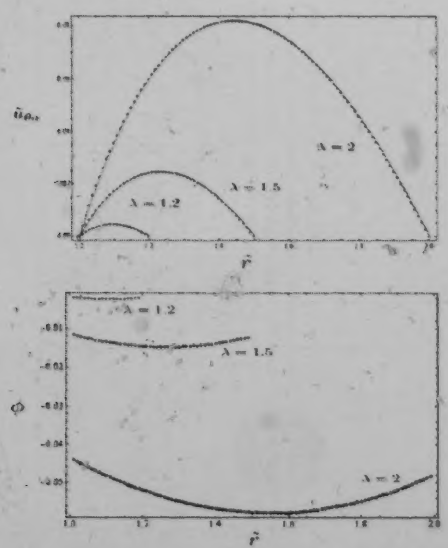

Figure 4.2: Low Womersley number, low Reynolds number: Non-dimensional velocity amplitude $\tilde{u}_\theta$ (Top) and phase angle distributions ϕ (Bottom) for three different aspect ratios ($\lambda = 1.2, 1.5, 2$) have been plotted for the low frequency oscillating flow solution (Womersley number, $\alpha = 0.1$) for a solid walled annulus (Radial Reynolds number, $\beta = 0$).

For an applied circumferential pressure gradient of the form

$$-\frac{\partial P}{\partial \theta} = K\rho\cos(\omega t) \tag{4.21}$$

the resulting non-dimensional periodic velocity is

$$\tilde{u}_\theta = \tilde{u}_{\theta a} \cos(\omega t + \phi) \tag{4.22}$$

where $\tilde{u}_{\theta a}$ and ϕ are the velocity amplitude and the phase angle respectively, both functions of the radial coordinate. $\tilde{u}_{\theta a}$ and ϕ can be determined as

$$\tilde{u}_{\theta a} = \left(\tilde{V}_r^2 + \tilde{V}_i^2\right)^{\frac{1}{2}} \quad , \quad \phi = \arctan \frac{\tilde{V}_i}{\tilde{V}_r} \tag{4.23}$$

where $\tilde{V}_r, \tilde{V}_i$ are the real and imaginary parts of $\tilde{V}$ (Equation 4.15). The general solution derived in the previous section can be reduced to the corresponding analytic solutions for non-porous walls given by Goldstein (steady, $\beta = 0$ and $\alpha = 0$, derived as Equation 4.5) and Tsangaris (oscillating, $\beta = 0$). The influence of the oscillation frequency and the amount of radial flux through the annulus on the velocity amplitude and phase angle distributions has been investigated by plotting Equation 4.15 for different combinations of the values of Womersley and Reynolds number.

4.3.1 Low frequency flows

Figure 4.2 (Top) shows the velocity amplitude for three different values of the aspect ratio (λ) with a reduced frequency (Womersley number α) of 0.1. The velocity amplitude has a parabolic profile behaving as a quasi-steady one resembling the velocity profile for a steady pressure gradient with a magnitude of $-K\rho\cos\omega t$. The phase-shift angle distributions

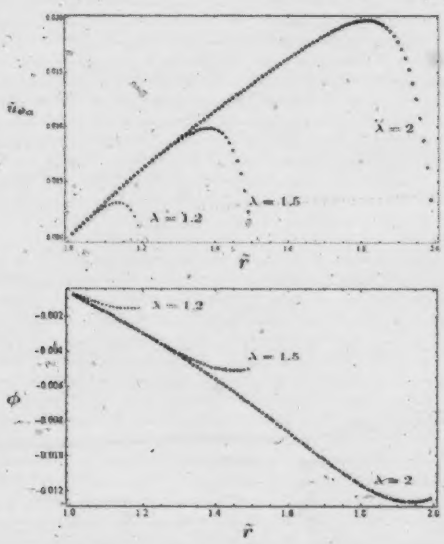

Figure 4.3: Low Womersley number, high Reynolds number: Non-dimensional velocity amplitude $\tilde{u}_\theta$ (Top) and phase angle distributions ϕ (Bottom) for three different aspect ratios ($\lambda = 1.2, 1.5, 2$) have been plotted for the low frequency oscillating flow solution (Womersley number, $\alpha = 0.1$) for a radially permeable annulus (Radial Reynolds number, $\beta = 30$).

have been plotted in Figure 4.2 (Bottom), and have values close to zero for the entire domain. The phase lag is symmetric over the flow region with minima near the walls. It can be inferred that viscous forces along with the inertial forces are quite significant in the flow region.

The velocity amplitude for the porous wall case with a high cross-flow Reynolds number ($\beta = 30$) and low oscillation frequency has been plotted in Figure 4.3 (Top). Comparing the velocity profile with the non-porous case, it can be deduced that the maximum velocity amplitude decreases with an increase in the cross-flow Reynolds number. It can be seen that the maximum in the velocity profile is shifted towards the suction wall, with a sharp

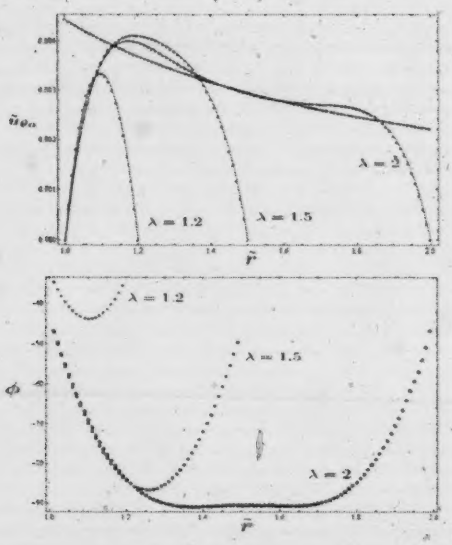

Figure 4.4: High Womersley number, low Reynolds number: Non-dimensional velocity amplitude $\tilde{u}_\theta$ (Top) and phase angle distributions ϕ (Bottom) for three different aspect ratios $(\lambda = 1.2, 1.5, 2)$ have been plotted for the high frequency oscillating flow solution (Womersley number, $\alpha = 15$) for a solid walled annulus (Radial Reynolds number, $\beta = 0$).

gradient in the suction region. Near the injection wall, the velocity profile is linear in nature, indicating an inviscid flow domain. However, the flow still remains unaffected by the oscillating aspect of the pressure field. It can be inferred that the flow near the injection wall is convection dominated and viscous effects are suppressed. In a very thin region near the suction wall, viscous forces are quite significant. This viscous region gets thinner as the cross-flow Reynolds number is increased, quite analogous to the viscous boundary layer diminishing in turbulent flows in pipes as Re increases. The phase shift angle (Figure 4.3 (Bottom)) has reduced from the no flux case and is no longer symmetric. The phase lag is almost zero at the injection wall because of the suppression of viscous forces, keeps increasing (more negative) until the region of maximum velocity and then recovers (less negative) a little near the suction wall.

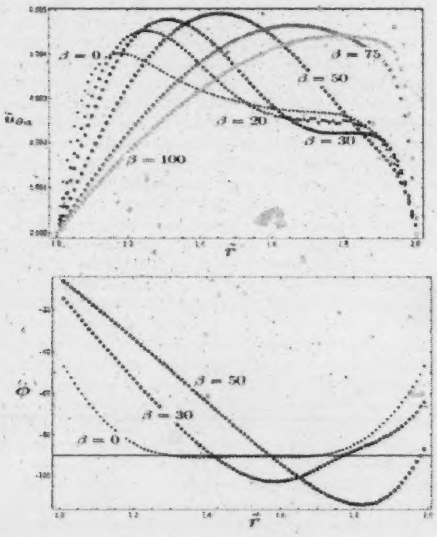

Figure 4.5: High Womersley number, high Reynolds number: Non-dimensional velocity amplitude $\tilde{u}_\theta$ (Top) and phase angle distributions ϕ (Bottom) for an aspect ratio of $\lambda = 2$ have been plotted for a high frequency oscillating flow solution with a Womersley number α of 15. The radial Reynolds number based on the radial velocity β ranges from 0 to 100 to study the convection effects in the flow region.

4.3.2 High frequency flows

Figure 4.4 shows the velocity amplitude and phase angle distributions for three different aspect ratios and a Womersley number of 15 for non-porous cylindrical annulus. The increase of oscillating frequency results in a reduction of the velocity amplitude and the velocity phase lags significantly from the applied pressure gradient. The velocity distribution exhibits a Stokesian character (very sharp gradients near the walls) and the annular effects (two local maxima in the velocity profile, maximum value close to the injection wall), also reported by Richardson and Tyler experimentally in [1], can be seen. The

phase angle in the central region tends to $-\pi/2$ and the fluid behaves as inviscid approaching the velocity profile of the inviscid pulsating flow, $\tilde{u}_\theta = \frac{1}{\alpha^2 \tilde{r}} \sin \omega t$. Near the walls, the phase angle tends to $-\pi/4$ and so does the stress phase lag.

The effect of cross-flow Reynolds number on high Womersley number (highly pulsating) flows can be seen in Figure 4.5 with the cross-flow Reynolds number (β) ranging from 0 to 100 with a reduced frequency (Womersley number, α) of 15. It can be seen that from the velocity profiles that as β increases the flattening effect of the velocity in the central region is reduced significantly and the maximum velocity shifts towards the suction wall. Annular effects disappear and the Stokesian nature of the velocity profile is diminished. The velocity amplitude first increases with β to a certain level and then falls off again as β increases beyond 50, where the flow is dominated by convection forces and viscous effects are suppressed. The phase angle increases (less negative, approaches zero) near the injection wall from the non-porous case and decreases (more negative than $-\pi/2$) in the central region recovering back (above $-\pi/2$) near the suction wall. This sinusoidal behavior of the phase lag is due to the new sinusoidal distribution in the velocity profile near the injection wall; however, on approaching towards the suction wall, this sinusoidal velocity region is suppressed by the viscous effects, bringing phase lag back to $-\pi/2$ and above. The flow near the injection wall can be approximated as unsteady convection-dominated inviscid flow.

From Equation 4.2 the radial pressure gradient can be determined as

$$\frac{\partial P}{\partial r} = -\frac{\rho A}{r^3}(\nu - A) + \frac{\rho u_\theta^2}{r} \tag{4.24}$$

Using the non-dimensional variables,

$$\frac{\partial \tilde{P}}{\partial \tilde{r}} = H\left(\frac{\tilde{u}_{\theta a}^2}{2\tilde{r}}\right)[1 + \cos(2\omega t + 2\phi)] + \left(\frac{1}{H}\right)\frac{\beta(\beta - 1)}{\tilde{r}^3} \tag{4.25}$$

where $\tilde{P} = P/K\rho$ and $H = KR_1^2/\nu^2$ is the ratio of pressure forces to the viscous forces. It can be seen that the radial pressure gradient oscillation frequency and the phase shift angle are double that of the corresponding frequency and phase angle of velocity oscillation. Also, an additional convective increment is superposed on the oscillating radial pressure gradient which further increments it towards the suction end.

4.4 Conclusions

The general solution for pulsating flow in an annulus with porous walls having a constant annular radial flux has been derived by solving the hydrodynamic equations assuming the finite gap approximation. Solutions for steady flow and oscillating flow with solid walls have been derived as limiting cases of the general solution. The solution for velocity amplitude and phase angle distribution has been plotted for low and high frequencies for variable flux conditions.

It is seen that for the low frequency case with no radial flux, parabolic velocity profiles are seen with small phase lags from the applied pressure gradient but as radial flux increases, convective effects start to dominate near the injection wall suppressing the viscous effects. The phase lag becomes unsymmetrical; starts from zero at the injection wall and decreases (more negative) towards the suction wall. In the high frequency case with no flux, annular effects are seen in the velocity profile which is Stokesian in nature and the phase lag decreases to a much larger extent than in the low frequency case with an asymptotic value of $-\pi/2$. With the increase of the radial flux, the annular effects disappear and the phase lag becomes unsymmetrical along the radial direction decreasing further beyond the asymptotic value. Convection effects are seen to dominate near the injection wall while viscous effects dominate near the suction wall. The solution will help in designing medical apparatuses with oscillating flows and oscillating mixing chambers.

References

[1] Richardson, E.G.; Tyler, E. *Proc. Phys. Soc.*, **1929**, 42, 1.

[2] Lamb, H. In *Hydrodynamics;*, Cambridge University Press. **1932**.

[3] Wang, C.Y. *ASME J. Appl. Mech.*, **1971**, 38, 553.

[4] Tsangaris, S.; Vlachakis, N.W. *J. Fluids Eng., Trans. ASME*, **2003**, 125, 382.

[5] Sexl, Th. *Z. Physik*, **1930**, 61, 349.

[6] Uchida, S. *J. Appl. Math. (ZAMP)*, **1956**, 7, 403.

[7] Dean, W.R. *Proc. Roy. Soc. London A*, **1928**, 121, 402.

[8] Goldstein, S. In *Modern Developments in Fluid Dynamics;* Clarendon Press, Oxford. **1938**, 315.

REFERENCES

[9] Tsangaris, S.; Vlachakis, N.W. *Applied Mathematical Modelling*, **2007**, 31, 1899.

[10] Womersley, J.R. *J. Physiol.*, **1955**, 127, 553.

[11] Drake, D.G. *Quart. J. Mech. Appl. Math.*, **1965**, 18(1), 1.

[12] Khamrui, S.R. *Bull. Cal. Math. Soc.*, **1957**, 49, 57.

[13] Tsangaris, S.; Vlachakis, N.W. *J. Appl. Math. (ZAMP)*, **2003**, 54(6), 1094.

[14] Bearman, A. S. *J. Appl. Phys.*, **1958**, 29(1), 71.

Chapter 5

Conclusion and Future Work

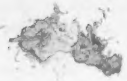

5.1 Conclusion

This thesis recommends the use of statistical mechanical models to understand macroscopic phenomena as a result of underlying interactions between the microscopic constituents of any system. Taking into consideration the complexity of statistical mechanical models, a thermodynamical application: evaporation of a liquid in a steady state system, and a fluid-mechanical application: pulsating flows in a rectangular duct, have been presented to give a more realistic assessment of physical systems.

Chapter 2 of the thesis presents a nonideal Statistical Rate Theory formulation for the evaporation of a liquid in a steady state system. Fluid nonidealities were incorporated in the previously existing ideal SRT formulation [1, 2] using equations of state and a generic equation-of-state based SRT model for liquid evaporation was developed. The Peng-Robinson equation-of-state based SRT model was taken as an example as the Peng-

5. Conclusion and Future Work

Robinson equation of state is fairly accurate for hydrocarbons, and it was found that it predicted evaporation rates as accurately as the ideal SRT model at low temperatures (below room temperature) and pressures (below 1 kPa). The calculated evaporation rates from both the SRT models were also concordant with the experimental results. Predictions based on the Peng-Robinson based SRT model were found to differ from the ideal SRT model at sufficiently higher temperatures and pressures (near the critical temperature). Experiments should be done in the near-critical region (temperatures higher than $0.8T_c$) to investigate the predictions that have been made. The generic equation of state based SRT model can be included in a thermodynamical simulator to predict evaporation rates at any range of temperature and pressure as the final expression is entirely in terms of experimentally measurable thermodynamic variables or the parameters of the equation of state which can be evaluated. Thus, being free from any fitting parameters and correlation, this is a very powerful tool for predicting evaporation rates.

Chapter 3 of the thesis presents the Lattice Boltzmann simulation details and results for pulsating flows in rectangular ducts due to a periodic pressure gradient using a 3-D Lattice Boltzmann model. It was found that at low frequencies of oscillation of the periodic pressure gradient, the velocity profiles are parabolic in nature behaving as velocity profiles for a steady pressure gradient. As the frequency is increased, annular effects start building up and the velocity profiles exhibit Stokesian character with annular effects and develop sharply near the wall and the central region of the duct behaves as an inviscid fluid approaching inviscid oscillating velocity profiles. The velocity phase lag behind the pressure gradient reaches its asymptotic value of $\pi/2$ in the central region and $\pi/4$ near the walls due to which stress lags by $\pi/4$ from the applied periodic pressure gradient. Stress was evaluated at different regions on the duct wall and it was found that stress is maximum in the middle of the duct walls and decrease to zero towards the corners. These results are concordant with the analytical solution derived by Drake. This leads us to a conclusion that LB models can be used to simulate pulsating flows in micro-sized ducts to analyze velocity and stress profiles in a duct. This information will be very useful for designing and optimizing medical apparatuses and to understand medical flow

phenomena, especially medical conditions like hypertension and dialysis.

Chapter 4 of the thesis discusses the exact solution of a pulsating flow in an annulus with porous walls having a constant annular radial flux. The hydrodynamic equations have been derived to obtain solutions for steady and oscillating flow in a duct with solid and porous walls. It was seen that for the low frequency case with no radial flux, parabolic velocity profiles are seen with small phase lags from the applied pressure gradient but as radial flux increases, convective effects start to dominate near the injection wall suppressing the viscous effects. In the high frequency case with no flux, annular effects are seen in the velocity profile which is Stokesian in nature but as radial flux increases, the annular effects disappear and the phase lag becomes unsymmetrical along the radial direction decreasing further beyond the asymptotic value of $-\pi/2$. Convection effects are seen to dominate near the injection wall while viscous effects dominate near the suction wall. The solution will help in designing medical apparatuses with oscillating flows and oscillating mixing chambers better.

5.2 Future work

Statistical Rate Theory assumes the evaporation process to be mainly a single-molecular event and thus neglects the probability of two or more molecules making the transition at the same instant. However, we can relax this assumption and evaluate the probability of two or more molecules making the transition, thereby obtaining an even more generic SRT model for evaporation. If we are able to do so, the methodology can be applied to other kinetic processes as well, like adsorption, and absorption, to name a few.

In the calculation of the equilibrium molecular exchange rate in the Statistical Rate Theory, it was assumed that classical kinetic theory can be used to obtain an expression for

the exchange rate. It was assumed that the number of collisions which increase or decrease the probability of a molecule to cross the interface are almost equal and so collisions do not affect the equilibrium molecular exchange rate. However, these assumptions can be relaxed. For example, we can use local density instead of global density while finding the probable number of molecules in a certain differential element which will cross the interface. This might involve the use of radial distribution functions and hence would be very complex to solve. Further, we can also define a collision operator very similar to the way it is defined in the Boltzmann equation, to correct for the collision effect on the equilibrium molecular exchange rate.

Further, as we predicted the evaporation rates for ethane and butane at near critical temperatures, experiments should be done in the temperature range and the predictions can be investigated. Temperature jump across the interface should be measured and checked with our assumption of choosing the temperature jump to be less than 2 K.

Lattice Boltzmann simulations for pulsating flow can be extended to curved geometries and grid refinement techniques can be used. For curved geometries, a different set of boundary conditions and stress evaluation techniques have been given in the literature [3, 4] and these can be used to investigate the asymptotic velocity profiles and to analyze stress at the curved geometry wall.

Although molecular dynamics is time consuming and computationally expensive, it can be employed to study these processes and can be compared with the results obtained from SRT and LB models. For example, a molecular dynamics study of the equilibrium molecular exchange rate can be done to check the expression that we obtain from the classical kinetic theory or the expressions that we can derive if we relax the assumptions as discussed earlier. A molecular dynamics simulation of pulsating flow in a pressure gradient can be carried out and the results can be compared with the LB simulation results.

Further, the analytical solution for pulsating flow with a radial flux in a porous annulus that was obtained in chapter 4 of the thesis can be compared with the Lattice Boltzmann simulation results of the problem. Again, curved geometry boundary conditions and grid refinements techniques would have to be used.

References

[1] Ward, C. A.; Fang, G. *Physical Review E*, **1999**, 59(1), 429.

[2] Fang, G.; Ward, C. A. *Physical Review E*, **1999**, 59(1), 441.

[3] Mei, R.; Yu, D.; Shyy, W.; Luo, L.S. *Physical Review E*, **2002**, 65, 041203-1.

[4] He, X.; Doolen, G. *Journal of Computational Physics*, **1997**, 134, 306.